Department of Physics and Astronomy
Heidelberg University

Bachelor Thesis in Physics
submitted by

Christian Amos Gölzhäuser

born in Heidelberg (Germany)

2021

Building a new Dy quantum gas experiment

This Bachelor Thesis has been carried out by
Christian Amos Gölzhäuser
at the
Physical Institute in Heidelberg
under the supervision of
Prof. Dr. Lauriane Chomaz

Abstract

In this thesis, some of the first design steps for a new quantum gas experiment with ultracold dysprosium atoms are presented. Dysprosium has the largest magnetic dipole moment of the periodic table. The goal is to cool and trap dysprosium atoms in a confined space as to then be able to tune the scattering length and the orientation of the strong dysprosium-specific magnetic dipole moment via an external magnetic field, in order to reach quantum states beyond the Bose-Einstein condensate. The experimental setup consists of a compact vacuum structure, into which hot dysprosium vapour is dispensed. The slowing and cooling mechanism comprises a 2D MOT working on a broad electronic transition, serving as a slow atom source and a 3D MOT working on a narrow electronic transition. It is the first time ever, that a 2D MOT is used on dysprosium. This thesis covers the turbulent first months of designing a new experiment. In particular, the custom design of some of the main vacuum parts a well as calculations on the vacuum quality itself and also the design of the magnetic field for the 2D MOT is presented.

Zusammenfassung

In dieser Arbeit werden einige der ersten Design Schritte für ein neues Quantengas Experiment mit Dysprosium Atomen präsentiert. Dysprosium besitzt das stärkste magnetische Dipolmoment des Periodensystems. Das Ziel ist Dysprosium Atome zu kühlen und in einem begrenzten Volumen einzufangen um dann mithilfe eines externen Magnetfeldes die Streulänge, sowie die Orientierung des starken Dysprosium spezifischen magnetischen Dipolmoments zu steuern um schließlich Quntenzustände jenseits des Bose-Einstein Kondensats zu erreichen. Der experimentelle Aufbau besteht aus einer kompakten Vakuumapparatur, in die ein heißer Strahl von Dysprosium Atomen insertiert wird. Der Entschleunigungs- und Kühlmechanismus umfasst eine 2D MOT, die an einem breiten elektronischen Übergang arbeitend als eine Quelle langsamer Atome dient und eine 3D MOT, die mit einem schmalen elektronischen Übergang fuktioniert. Es ist das erste Mal überhaupt, dass eine 2D MOT mit Dysprosium realisiert wird. Die Arbeit zeigt einige Resultate der turbulenten ersten Monate der Designphase eines neuen Experiments. Speziell wird das Design einiger der wichtigen Vakuumbauteile, sowie einige Berechnungen über die Vakuumqualität selbst sowie das Design des Magnetfeldes der 2D MOT präsentiert.

Contents

1 Introduction 3
- 1.1 Motivation . . . 3
- 1.2 Tuning ultracold quantum gases . . . 3
- 1.3 Dipolar Interactions . . . 3
- 1.4 Dysprosium . . . 4

2 Theory of Magneto-optical trapping 5
- 2.1 Atom light Interaction . . . 5
- 2.2 Doppler effect . . . 7
- 2.3 Zeeman effect . . . 7
- 2.4 Optical molasses . . . 7
- 2.5 MOT . . . 9
- 2.6 Capture velocity and loading rate . . . 10

3 Experimental setup of the new experiment 11
- 3.1 Atomic beam source . . . 12
- 3.2 2D MOT chamber . . . 13
  - 3.2.1 Magnetholders . . . 16
- 3.3 Other custom vacuum parts . . . 17
  - 3.3.1 Pushing and pumping stage . . . 17
  - 3.3.2 Differential pumping stage . . . 19
  - 3.3.3 Connector box . . . 20
- 3.4 Assembly and Mounting . . . 21

4 Vacuum 22
- 4.1 Molecular flow theory . . . 23
- 4.2 Vacuum pumps . . . 24
  - 4.2.1 Prepumping . . . 24
  - 4.2.2 Ion-Getter pumps . . . 25
- 4.3 Vacuum simulations . . . 26
- 4.4 High vacuum . . . 27
- 4.5 Ultra high vacuum . . . 29
- 4.6 Differential pumping . . . 29
- 4.7 Conclusion . . . 31

5 Magnetic field of the 2D MOT 33
- 5.1 Permanent magnets . . . 34
- 5.2 Position scanning . . . 35
  - 5.2.1 Four magnets . . . 35
  - 5.2.2 Eight magnets . . . 37
- 5.3 Asymmetric arrangements . . . 41
- 5.4 Unwanted effects . . . 42

6 Conclusion and Outlook 43
- 6.1 Conclusion . . . 43
- 6.2 Outlook . . . 44

1 Introduction

1.1 Motivation

In our Dysprosium lab, our goal is to build a new compact and modular experimental setup, aimed to produce and observe degenerate quantum gases of Dysprosium atoms in a tunable assembly concerning dimensionality and geometry. Since Dysprosium is in fact the most magnetic element of the periodic table, it is ideally suited to observe long-range anisotropic magnetic dipole-dipole interactions between the atoms. Such interactions are intensified to a sizable level, compared to regular contact interactions with a shorter range, due to the strong magnetic dipole moment of the Dysprosium ground state. The concept of the new experiment is to build a 2D MOT and use it as a collimated beam source for slow Dy atoms in a high vacuum environment and after that capture them in a 3D MOT and evaporatively cool them further in an ultra-high vacuum environment. This thesis is mainly focused on three aspects of the experiment, which are of major importance for producing degenerate quantum gases of heavy alkaline-earth like atoms. One needs an ultra-high vacuum such that there will be limited unwanted collisions with other particles, one needs a well designed magnetic field with suitable gradients in order to apply the magneto-optical trapping scheme and last but not least, one needs a custom mechanical design for many parts of the experimental setup, to meet all the requirements to produce an ultracold quantum gas.

1.2 Tuning ultracold quantum gases

In nature, most systems that we know are governed by the collective behaviour of particles, whether in solids, liquids or gases. Quantum theory predicts these dynamics to give rise to a variety of yet unknown quantum states and excitations. These dynamics however are nearly impossible to study in a condensed matter environment due to overlaying effects like phonon lattice dynamics and disorder in general. Moreover, it is difficult to precisely control such a system. This is where the ultracold quantum fluid comes into play. Since the first realization of a Bose-Einstein condensate in 1995, many experiments have been able to successfully study quantum phenomena in an ultracold environment produced by laser light and magnetic fields. The quantum gases are realized in very low densities and can be well controlled. In that way the system can be used for example as a quantum simulator for a variety of Hamiltonians. Other than the first Bose-condensed alkali-species, which interact mainly through short range contact, the realization of a degenerate ultracold quantum fluid of atoms with a large magnetic dipole moment offers the opportunity to study long range anisotropic dipolar interactions.

1.3 Dipolar Interactions

The long range interaction potential of two magnetic dipoles induced by an external field can be described in the following manner:

$$V_{dd}(r,\theta) = \frac{\mu_0 \mu_m^2}{4\pi} \frac{1 - 3\cos^2\theta}{r^3} \tag{1.1}$$

where r is the distance between the dipoles and θ is the angle between the axis of the external field and the direction towards the other dipole $\mathbf{r}$. The dependence on θ makes the interaction anisotropic and it can even be either repulsive or attractive. In a head-to-tail orientation the interaction is attractive, whereas it is repulsive if the dipoles are oriented side by side. Because of these fundamental properties of the dipole-dipole interaction, it has been predicted that dipolar quantum gases will lead the path to a variety of interesting exotic quantum phenomena. However, in order to realize a quantum gas with significant dipole-dipole interactions, one needs particles with either a strong electric dipole moment d or a strong magnetic dipole moment μ_m. The problem with electric dipoles is that even though there are molecules with large electric dipoles, in many cases the dipole is not permanent and it is very difficult to cool such molecules down to quantum degeneracy. In our experiment we will focus on atoms with a high magnetic moment μ_m.

1.4 Dysprosium

Dysprosium is a lanthanide with atomic number 66. It appears naturally in mainly four different isotopes, two bosonic and two fermionic and has the highest magnetic dipole moment of the currently known periodic table, which makes it one of the most obvious choices for realizing a dipolar quantum gas. The magnetic moment of dysprosium in its electric ground state is $10\mu_B$, it can be explained since there are unpaired electrons in a state with high angular momentum. The electronic configuration of the ground state is [Xe]4f^{10}6s^2. In the f orbital there are four unpaired electrons which therefore make up an orbital angular momentum of $L = 6$ and a total angular momentum of $J = 8$ in the ground state. In spectroscopic notation the ground state would therefore be written as $^5\mathrm{I}_8$. At low pressures, dysprosium will start to sublimate approximately above 1100°C, depending on the required vapour pressure (see [19]) and create a vapour, even though the melting point is at 1412°C.

isotope	^{161}Dy	^{162}Dy	^{163}Dy	^{164}Dy
Atomic mass [u]	161	162	163	164
Abundance [%]	18.9	25.5	24.9	28.3
Statistics	fermionic	bosonic	fermionic	bosonic

Table 1: Abundances and properties of dysprosium isotopes

For the cooling process the electronic transitions are particularly relevant. During the deceleration and cooling process through laser light we will use two specific transitions. The one which will be used for the first cooling and deceleration stage goes from the ground state to the 4f^{10}6s6p ($^1P_1$) singlet state. Due to the wavelength of about 421 nm, this will be called the 'blue transition'. For the second laser cooling stage, the $^3P_1$ triplet state with the same electron configuration will be used. It has a wavelength of 626 nm and will therefore be referred to as the 'red transition'. What is relevant for a cooling stage using laser light is especially the transition rate Γ and the directly related natural linewidth $\Delta\nu$. The following table offers an overview over the parameters of the two specific transitions that will be targeted. Using a broad transition makes it possible to capture more atoms also with higher velocity, but limits the temperature to which they can be cooled down. A narrow transition enables cooling to lower temperatures but the maximum velocity at which atoms can be captured is smaller, thus only few atoms qualify as targets. For other dysprosium properties that are crucial for cold atom experiments, see also [16].

		$^5I_8 \rightarrow ^1 P_1$	$^5I_8 \rightarrow ^3 P_1$
Wavelength [nm]	λ	421.290	626.082
Natural linewidth	$\Delta\nu$	32.2 MHz	135 kHz
Lifetime	τ	4.94 ns	1.2 μs
Saturation intensity	I_{sat}	56.4 $\frac{\mathrm{mW}}{\mathrm{cm}^2}$	72 $\frac{\mu\mathrm{W}}{\mathrm{cm}^2}$
Landé factor (excited state)	g_J*	1.22	1.29

Table 2: Overview of some important parameters specific to dysprosium

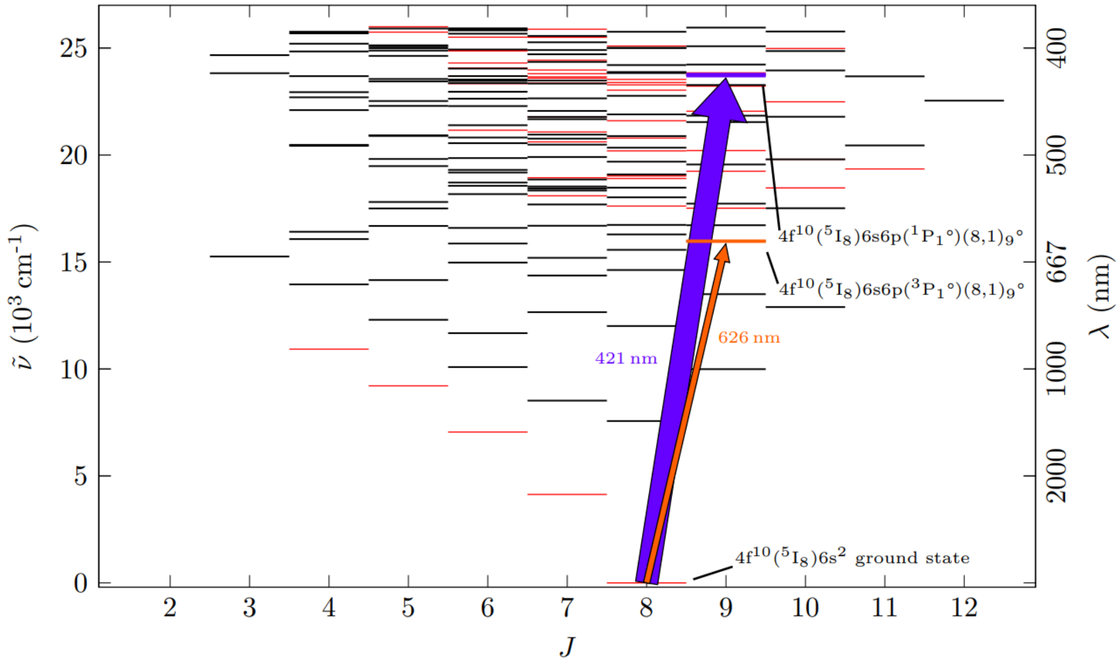

Figure 1: Energy level diagram of dysprosium. The broad blue transition and the narrow red transition which will be used are highlighted. Figure from [15]

2 Theory of Magneto-optical trapping

To produce ultracold gases from a hot vapour we will apply magneto-optical trapping. The hot vapour is collimated into an atomic beam and fed into the vacuum chamber of our experimental setup. In our first trap, namely the 2D MOT, the atoms are then decelerated by an arrangement of counterpropagating laser beams and pushed towards the centre of the first vacuum chamber, where they will be spatially confined through a force field created through laser beams and permanent magnets and cooled down further. Note, that as the name suggests, the cooling and confinement mechanism works only in two dimensions here. After the 2D MOT, the atoms are transported to a 3D MOT in the science chamber and from there loaded into an optical dipole trap. The 2D MOT therefore simply serves as a source of slow atoms, since the atoms in the atomic beam coming from the oven could not be captured in the 3D MOT. Some good and much more detailed references on the trapping mechanism used for this experiment and described in this chapter are [21] and [9].

2.1 Atom light Interaction

It is assumed that the atom is point-like and has a ground state $|g\rangle$ and an excited state $|e\rangle$. The difference in energy between these two states is $E = \hbar\omega_{eg}$. What is also important is the spontaneous emission rate of the transition $\Gamma = \frac{1}{\tau}$ with τ being the lifetime of the excited state. The laser light with which the atom will interact will be treated in the classical plane wave approximation. The main parameters by which the light is characterized are the polarization vector $\mathbf{e}$, the wave vector $\mathbf{k}$ and the frequency ω. The electric field can then be written as:

$$\mathbf{E}(\mathbf{r}, t) = E_0 \mathbf{e} cos(\omega t - \mathbf{kr}) \tag{2.2}$$

From here we can use the approach of the so called Optical Bloch Equations [21], which allow us to quickly derive an expression for the net force exerted onto an atom along the laser beam. The

Hamiltionian used to describe the two energy level system and the interaction with the electric field of the laser system can be written as:

$$H = \hbar\omega_{eg} \left|e\right\rangle \left\langle e\right| - \mathbf{dE} \tag{2.3}$$

with **d** being the atomic dipole operator and **E** being the electromagnetic field just as before. At this point it makes sense to introduce the Rabi frequency. Being defined as:

$$\Omega = -\frac{\mathbf{dE}}{\hbar} \tag{2.4}$$

This describes the atom light coupling. The optical Bloch approach then uses the density matrices, describing the ground state, excited state and coherent state populations, and relates them in four differential equations, the optical Bloch equations:

$$\begin{aligned} \frac{d\rho_{gg}}{dt} &= \Gamma\rho_{ee} + \frac{i}{2}(\Omega^*\bar{\rho}_{eg} - \Omega\bar{\rho}_{ge}) \\ \frac{d\bar{\rho}_{ge}}{dt} &= -(\frac{\Gamma}{2} + i\Delta)\bar{\rho}_{ge} + \frac{i}{2}\Omega^*(\rho_{ee} - \rho_{gg}) \\ \frac{d\bar{\rho}_{eg}}{dt} &= -(\frac{\Gamma}{2} - i\Delta)\bar{\rho}_{eg} + \frac{i}{2}\Omega^*(\rho_{gg} - \rho_{ee}) \\ \frac{d\rho_{ee}}{dt} &= -\Gamma\rho_{ee} + \frac{i}{2}(-\Omega^*\bar{\rho}_{eg} - \Omega\bar{\rho}_{ge}) \end{aligned} \tag{2.5}$$

We have already introduced some important parameters here, another one is the detuning $\Delta = \omega_{eg} - \omega_{laser}$. It is the difference in frequency between the laser and the atomic transition. Furthermore $\bar{\rho}$ stands for $\rho e^{-i\Delta t}$ and Ω^* denotes the complex conjugate of Ω. Solving for a steady state solution, which means setting the time derivative to zero, yields the following expression:

$$\rho_{ee} = \frac{I/2I_{sat}}{1 + I/I_{sat} + (2\Delta/\Gamma)^2} \tag{2.6}$$

Here, I is the laser intensity and I_{sat} is the saturation intensity of the specific resonance.

$$I_{sat} = \frac{\pi hc\Gamma}{3\lambda^3} \tag{2.7}$$

In the following, the relation of the two will simply be given by the on-resonance saturation parameter $s_0 = \frac{I}{I_{sat}}$. Once we found the steady state solution we can easily obtain an expression for the scattering force. When the atom absorbs a photon from the laser beam, there will be a transition of the momentum $\hbar k$ from the light beam to the atom. When the atom then spontaneously emits a photon, momentum transfer occurs again. Spontaneous emission is isotropic, thus the momentum transferred onto the atom balances out after a few emission events and on average, the atom is not pushed anywhere through spontaneous emission alone. However, the absorption always occurs in the same direction, which is why it can be said that a net force acts on the atom along the laser field:

$$\mathbf{F}_{sc} = \hbar\mathbf{k}\Gamma\rho_{ee} = \frac{\hbar\mathbf{k}s_0\Gamma/2}{1 + s_0 + (2\Delta/\Gamma)^2} \tag{2.8}$$

This is also called the radiation pressure since it describes how during the whole absorption-emission process a net pressure is acting on the atoms and pushing them in a certain direction. For high intensities, i.e. $s_0 >> 1 + (2\Delta/\Gamma)^2$, the radiation pressure will converge to its maximum at $\mathbf{F}_{max} = \hbar\mathbf{k}\Gamma/2$. If the intensity is then increased further, atoms with higher velocity can be trapped, or in other words, the so-called capture velocity is increasing. This leads us directly to the next section of this chapter.

2.2 Doppler effect

For now we have taken the simplest possible assumptions in order to understand how to decelerate, cool and trap neutral atoms. We will now step by step add a few features which need to be considered for our experimental setup, until we arrive at our 2D MOT. In the previous part we have looked at how absorption and emission will influence an atom's momentum, but have not considered the initial velocity of the atom. The initial velocity however plays a major role since the effective detuning Δ' will be shifted from the 'normal' detuning due to the Doppler effect. Since the atoms velocity will obviously change during the deceleration process, the effective detuning will also be continuously changing.

$$\Delta' = \Delta - \mathbf{kv} \tag{2.9}$$

To efficiently trap and cool atoms, one usually has to account for the Doppler shift.

2.3 Zeeman effect

A measure to account for or compensate this velocity-dependent effect is to apply a magnetic field, which would induce a splitting in energy levels for a degenerate state. This splitting would once more change the effective detuning, depending on the magnetic field strength. Thus the compensation could also be set up in a position-dependent manner by varying the magnetic field strength in different regions. The most common method of achieving this result used to be a so called Zeeman-slower, which consists of a series of coils in which the number of windings varies from stage to stage. This setup then tunes the atomic level separation also, known as the Zeeman effect. The different stages produce a spatially varying magnetic field, and the resulting energy shift can compensate the Doppler shift.

$$\Delta' = \Delta - \mathbf{kv} + \frac{g_J * \Delta m_J \mu_B}{\hbar} B(\mathbf{r}) \tag{2.10}$$

Here Δm_J denotes the difference in the momentum projection quantum number along the axis of quantization, between the ground state and the excited state. Due to selection rules, Δm_J can only be either -1,0 or 1. Here g_J* is the Landé factor of the excited state. Many existing ultracold atom experiments use Zeeman slowers as a method to increase their overall loading rate by compensating the Doppler shift of high velocity atoms, such that they are then on resonance with the laser beam. Our experimental setup however is designed to work without a Zeeman slower, but relies on a 4-laser beam 2D MOT. Here, we plan to invest in high laser light intensity and also increase the capture velocity in that way.

2.4 Optical molasses

We now want to have a closer look at the effect of two counterpropagating laser beams on an atom. Those beams have the same detuning and intensity saturation. We assume them to act independently on the atom. In that case we can simply add the scattering forces together:

$$\mathbf{F} = \frac{\hbar \mathbf{k} \Gamma}{2} \left(\frac{s_0}{1 + s_0 + (2(\Delta - \mathbf{kv})/\Gamma)^2} - \frac{s_0}{1 + s_0 + (2(\Delta + \mathbf{kv})/\Gamma)^2} \right) \tag{2.11}$$

In this beam configuration, the constant terms of the radiation pressure cancels out. What is left can be approximated for small velocities through a Taylor expansion and then looks like a simple friction force:

$$\mathbf{F} \approx \frac{8\hbar k^2 \Delta/\Gamma s_0 \mathbf{v}}{(1 + s_0 + (2\Delta/\Gamma)^2)^2} := -\beta \mathbf{v} \tag{2.12}$$

Here β would be the damping coefficient. We want an atom with a given direction to be decelerated by counterpropagating light, therefore one can quickly see that the detuning Δ needs to be negative or 'red-detuned'. If an atom now moves into a light field consisting of counterpropagating beams, it will perceive the beam propagating into the opposing direction as Doppler shifted towards resonance and thus be more affected by this beam. Due to the choice of the detuning the radiation pressure can then act as a friction force and decelerate the atoms and thereby cool down the atom cloud. Remember, that the temperature of the gas T is proportional to its mean square velocity $< v^2 >$. This setup is also called optical molasses. While the friction force cools the atoms down, the spontaneous emission of light, which occurs randomly induces heat, which is why there is a temperature limit at which these opposing processes are in balance and the atoms can not be cooled any further. This so called Doppler temperature can be derived through the reduction and growth rates of the kinetic energy, i.e. $< v^2 >$, caused by the cooling and heating processes and the virial theorem:

$$T_D = \frac{\hbar\Gamma}{2k_B} \tag{2.13}$$

For the Doppler temperature we need $\Delta = 2\Gamma$. Note, that other cooling techniques can bring the temperature of the atom cloud below the Doppler limit, close to the so called recoil limit. The recoil limit corresponds to the energy transferred from the spontaneous emission of a single photon onto the atom. It is thus only dependent on the wavelength of the transition.

$$T_{RC} = \frac{\hbar^2 k^2}{2mk_B} \tag{2.14}$$

In the main chamber of the experiment evaporative cooling [9] will be used to reduce the temperature further.

Let us now look for a moment at our specific case of Dysprosium. In the 2D MOT we plan to use the transition $4f^{10}6s^2 \rightarrow 4f^{10}6s6p$ ($^5I_8 \rightarrow ^1 P_1$) with a wavelength of $\lambda_{blue} = 421.291$ nm and a transition rate of $\Gamma_{blue} = 33.157 \times 2\pi$ MHz. The transition rate or the natural linewidth of this 'blue' transition is relatively large and thus produces a high radiation pressure, which is useful for initial cooling. But at the same time the Doppler limit temperature is comparably large:

$$T_{D,blue} = 0.796\,\mathrm{mK} \tag{2.15}$$

Therefore for further cooling, we will use the $^5I_8 \rightarrow ^3 P_1$ transition with $\lambda_{red} = 626.086$ nm and $\Gamma_{red} = 0.1421 \times 2\pi$ MHz in a 3D MOT. This will be called the 'red' transition. Now the Doppler limit reduces to

$$T_{D,red} = 3.411\,\mu\mathrm{K} \tag{2.16}$$

but further cooling may allow for temperatures close to the recoil limit

$$T_{R,red} = 148\,\mathrm{nK} \tag{2.17}$$

However the narrow linewidth of this transition weakens the scattering force and makes the overall cooling less efficient, which is why it would be very ineffective to use a narrow line transition for initial cooling of the collimated beam of hot atoms.

2.5 MOT

So far it has been discussed how to decelerate and cool atoms efficiently, but in order to trap them, they need to be spatially confined, which is not possible with cooling beams alone, since the cooling process works the same way independent of space. To create a well defined capture region, we have to combine the optical molasses with an inhomogeneous magnetic field. As mentioned earlier, a magnetic field induces Zeeman-splitting of the degenerate energy levels of the dysprosium atom and changes the detuning such that the scattering force depends on the magnetic field strength that is varying in space. This allows us to create a spatially confined capture region. Let us for a moment once again consider the two eigenstates $|g\rangle$ and $|e\rangle$ and assume for simplicity that they are described by the quantum numbers $J = 0$ and $J = 1$. Now for the magnetic field we choose a linearly changing field along the $\mathbf{x}$ direction. With the magnetic field gradient b, we can describe the field in the following way:

$$\mathbf{B} = b\mathbf{x} \tag{2.18}$$

The energy difference due to the induced Zeeman splitting of the degenerate energy levels in the $J = 1$ state is then linearly dependent on the x-position:

$$\Delta E = g_J m_J \mu_B b x \tag{2.19}$$

This is where the polarization of the laser beams, which was not yet mentioned, comes into play. Due to selection rules, σ^+ polarized light can only trigger transitions where $\Delta m_J = 1$ and σ^- polarized light can only drive $\Delta m_J = -1$ transitions. In other words, the polarization of the light changes the sign of the energy shift in equation 2.19. The full expression of the scattering force with counterpropagating beams in a configuration, in which one beam has σ^+ and one has σ^- polarization, looks as following:

$$\begin{aligned}\mathbf{F}_{sc} = \frac{\hbar \mathbf{k} \Gamma}{2} (& \frac{s_0}{1 + s_0 + (2(\Delta - kv - \mu_B g_J m_J b x/h)/\Gamma)^2} \\ & - \frac{s_0}{1 + s_0 + (2(\Delta + kv + \mu_B g_J m_J b x/h)/\Gamma)^2})\end{aligned} \tag{2.20}$$

Now one can build the MOT in a way, that the atom will always be pushed to the centre of the chamber. If we for example assume the atom to be at a position $x > 0$ and have no velocity, the transition with Δm_J will be pushed towards resonance due to the Zeeman splitting. Therefore a σ^- polarized beam in negative x-direction will push the atom back to the centre. The analoge process takes place for an atom at $x < 0$. As in the chapter on optical molasses, the total radiation pressure can also be approximated for small velocities in a similar way, now with the additional Zeeman term:

$$\mathbf{F}_{sc} = -\beta \mathbf{v} - \kappa \mathbf{x} \tag{2.21}$$

with

$$\kappa = \frac{g_J \mu_B b}{\hbar k} \beta \tag{2.22}$$

Here we can clearly differentiate between the cooling part, described in the optical molasses, and the spatial confinement part. Through this approximation one can also find that the dynamics of our 2D MOT are in principle the same as those of a damped harmonic oscillator, which intuitively makes sense considering that the goal of the whole apparatus is to decelerate and confine moving particles.

Until now we have only been talking about counterpropagating beams in general. In the 2D MOT it is planned to realize this with a single beam, that is lead through the chamber in a configuration roughly resembling a 'bow-tie'-like shape, which can be seen below. Since we then have two sets of counterpropagating beams, they form a two-dimensional plane, hence the name 2D MOT. In the 3D MOT, even though, the beam path is not fully worked out yet, we will have three sets of counterpropagating beams, spanning in three-dimensional space.

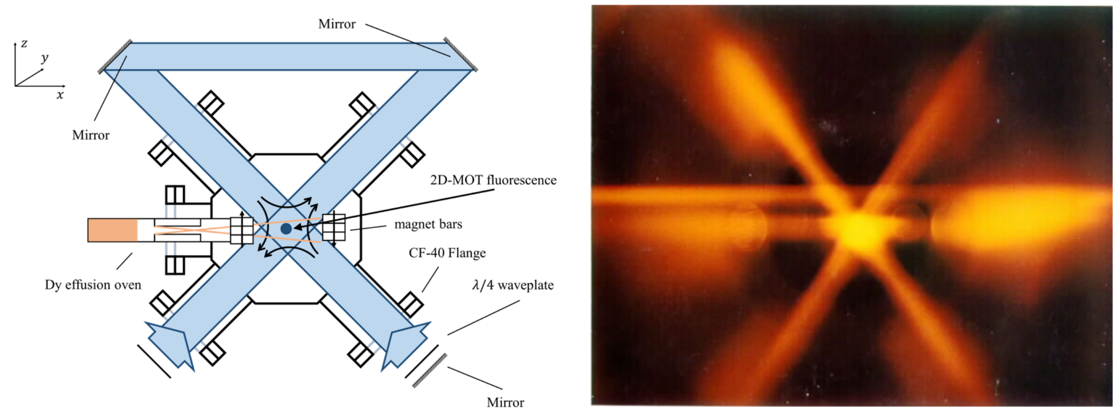

Figure 2: On the left a schematic drawing of how the laser beams are arranged for the 2D MOT. On the right an image of optical molasses of sodium atoms in a 3D MOT, realized in the group of W.D. Phillips at NIST, USA. Image adapted from [5].

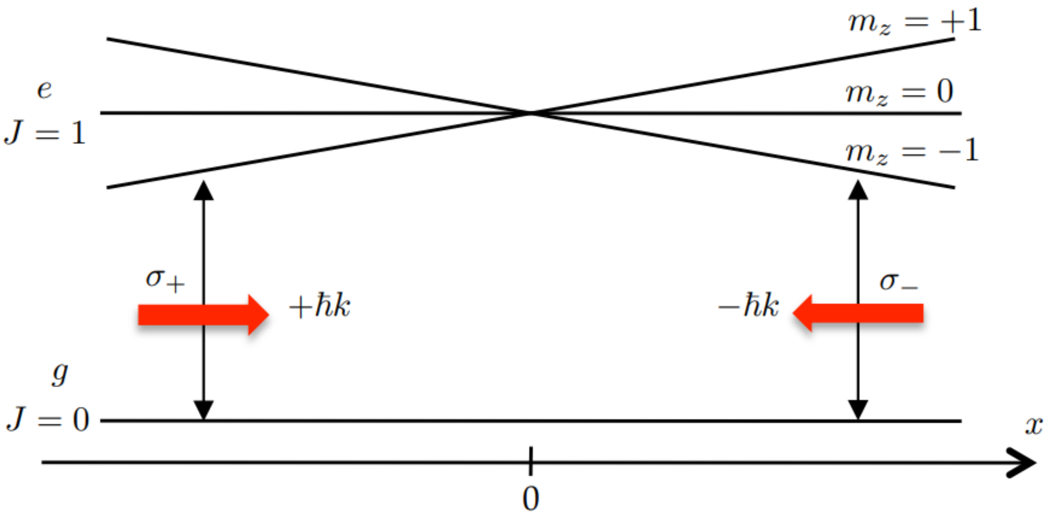

Figure 3: Schematic drawing of the MOT mechanism. The solid black lines show the energy of the different atomic sublevels in the magnetic field. Due to the polarization arrangement of the cooling beams and selection rules, atoms are pushed towards the centre. Figure taken from [5]

2.6 Capture velocity and loading rate

As mentioned before, the dysprosium atoms are dispensed from an oven into the 2D MOT chamber, and form an atomic beam from which they are loaded into the capture region. The beam follows a three-dimensional Maxwell-Boltzmann distribution, which means the velocities of the single atoms are distributed around the root mean squared velocity for atoms with mass m and temperature T. Not all velocities can be captured. Due to the finite dimensions of the chamber only those atoms are considered which are slow enough such that they only have to pass through relatively few absorption-emission cycles until they are slowed down to an extent that they no longer can leave the capture region. That is why there is a cutoff velocity which in this context is called capture velocity v_{cap}. In general, only atoms slower than the capture velocity can be trapped. The exact calculation of the capture velocity shall not be the topic of this section. Just note, that it is proportional to the square of the linewidth Γ of the transition. So the broader the transition, the higher the capture velocity. It is therefore vital, that we slow the atoms with a broad transition in the 2D MOT, so that in the 3D MOT they are already 'pre-slowed' so to say and can be captured using the more narrow red transition. If we take our case as an example once more, the melting point of Dysprosium is at 1412°C. Assuming the atomic beam has a temperature of around 1000°C, this results in a mean velocity of well over 400 m/s. Our simulation results for different Δ, s_0 and b have shown that the capture velocity will be only a fraction of that. The number of atoms captured, or loaded into the 2D MOT per second is called the loading rate L. It can be calculated by integrating over the Maxwell-Boltzmann distribution $f(v)$ from zero velocity until the capture velocity and multiplying with the atomic density n and the trapping cross section area S.

$$L_{MOT} = nS \int_0^{v_{cap}} v f(v) dv \tag{2.23}$$

The earlier mentioned simulations were conducted to scan for the best parameters to maximize the loading rate, while maximizing the loading rate mostly means maximizing the capture velocity. The underlying code of the simulations was written, and multiple times adapted to new developments, by our PhD student Jianshun Gao, see also [1].

3 Experimental setup of the new experiment

In the following chapter, our experimental setup will be described in more detail, especially focusing on the custom designed parts. Since the described deceleration and cooling techniques are nothing new in principle, there is a variety of other experiments, that use a similar experimental setup. A 2D MOT with dysprosium though has never been realized before, i.e., although we had many references for similar setups, they all had to be slightly adapted or even redesigned from scratch for our experiment. At the University of Heidelberg, the groups of Fred Jendrzejewski and Selim Jochim have been building conceptually similar cold atom experiments [14] [13], which continuously have served as a source of inspiration for us. The Na-K experiment in Prof. Jendrzejewski's group deals with the generation of ultracold mixtures of sodium and potassium atoms, while in Prof. Jochim's group, lithium fermions are cooled in the new experiment, also called 'HQA' for 'Heidelberg Quantum Architecture'. For experiments with alkaline-earth like atoms, the works of Matteo Barbiero at the Politecnico di Torino (Sr) [1], Philipp Ilzhöfer at the University of Innsbruck (Er-Dy mixture) [15], as well as those of Jeff Thompson's group at Princeton University (Yb) [25] have also provided some vivid examples for various parts of our experimental setup. However, the most distinct properties of dysprosium are its high melting point and the existence of a very broad transition, which means from this point of view actually rubidium or caesium would be the most similar atomic species.

The whole setup in general is divided into two parts, the high vacuum part and the ultra high vacuum part. In the high vacuum part, we plan to initiate the slowing and cooling process of hot dysprosium atoms coming from the oven, in the ultra high vacuum part, the atoms are cooled further and can be imaged. The core of the high vacuum part is the custom designed 2D-MOT chamber. The dysprosium oven, is attached to one side of the chamber in a way that the initial hot atomic beam enters the chamber horizontally and perpendicular to the main axis of the experiment

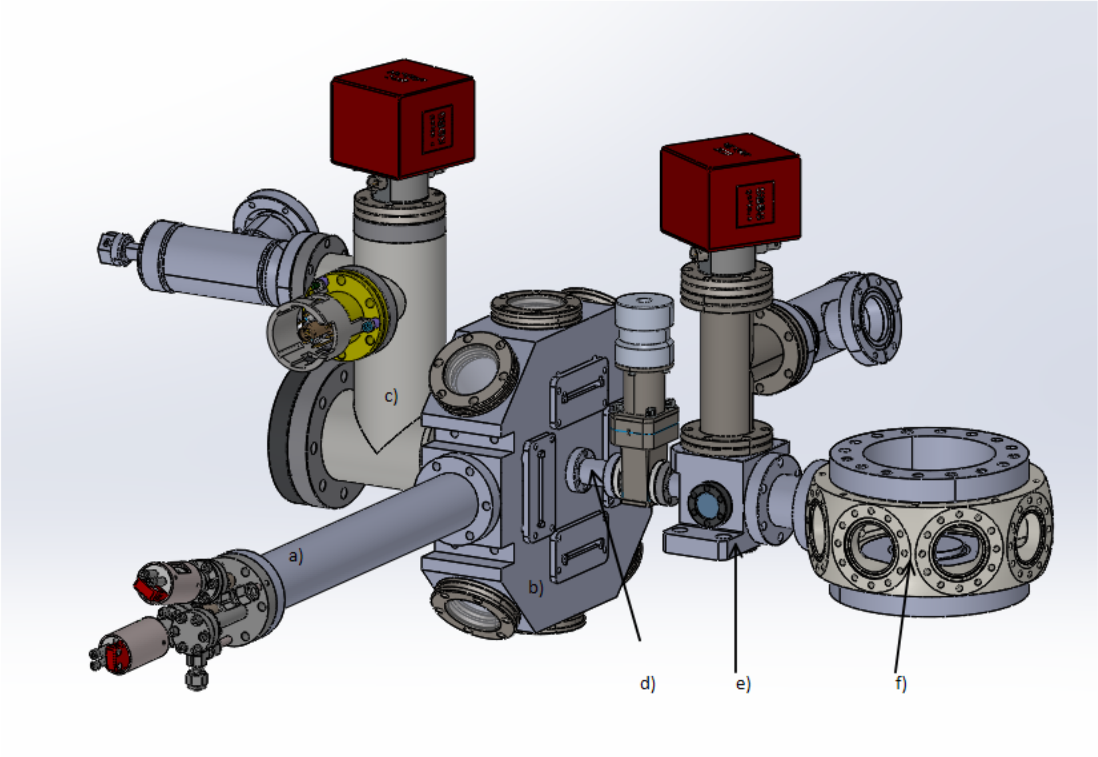

Figure 4: 3D model of the assembly of the vacuum components (without optical setup or mounting), with a) the atomic beam source, b) 2D MOT chamber, c) pumping and pushing stage, d) differential pumping stage, e) connector box to f) the main chamber.

(see a) in Figure 4). A pumping stage is connected to the 2D MOT chamber, that also provides optical access to insert a laser beam that can push through the capture region of the 2D MOT itself and accelerate the atoms into the next chamber in a controlled manner. The ultra-high vacuum part of the experiment is connected through a so called differential pumping stage (DPS), which is simply a narrow connection with a very low flow conductance, so that different pressures can be maintained on each side of the narrow tube. However, if the pushing beam is aligned well, the dysprosium atoms can be pushed through the DPS. The ultra high vacuum side also has a pumping stage, shaped like a little box and is therefore referred to as the 'connector box' in Figure 4. It connects through a short adapter tube to the main science chamber. Here during the first intermediate time stage of our experiment there will be a metallic chamber with large optical access, later we plan to attach a glass cell there. Anyhow, there is a 3D MOT in that science chamber, which allows us to use a narrow transition to recapture the 'pre-slowed' coming out of the 2D MOT and cool them further. The smaller linewidth reduces the temperature limit of the MOT. From the 3D MOT, the atoms will be loaded to conservative dipole traps and evaporatively cooled even further to reach quantum degeneracy.

3.1 Atomic beam source

The oven from which the atomic beam of dysprosium is dispensed into the chamber is itself a relatively large structure. The atomic beam source, as the oven is also called, works in the following manner: In a crucible the solid material is heated up to more than 1000°C. This is not the melting temperature of dysprosium (1421°C), but already at such temperatures material starts to sublimate, since the vapour pressure reaches a sizable value. The vapour then passes through some nozzles, which are simply apertures to shape the beam geometrically as can be seen in Figure 5, before

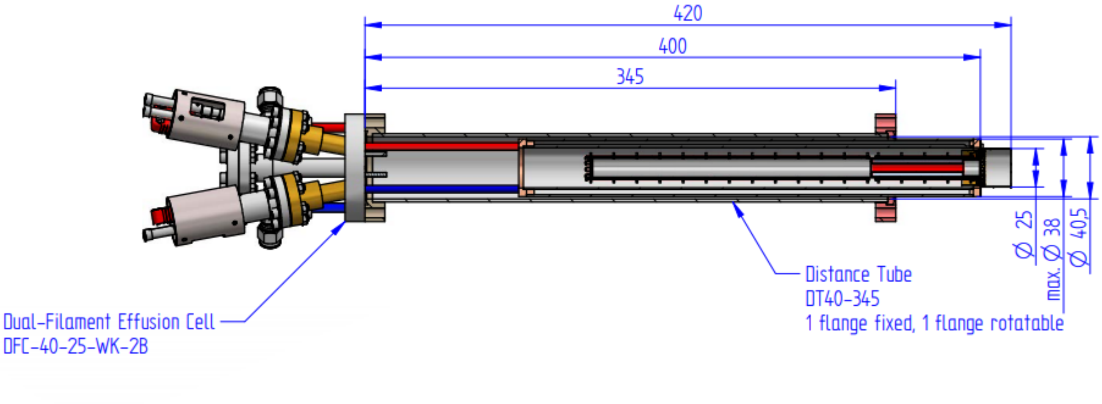

Figure 5: Drawing of the oven with the custom connector, provided by Createc Fischer & Co. GmbH.

leaving the oven through the final aperture. The diameter of the opening at the oven tip is 5.2 mm. It collimates the atomic beam further to allow for a maximum divergency angle of 15°, such that the beam cone will not hit any viewports on the opposite side of the 2D MOT chamber and coat them from the inside. The collimating apertures in the effusion cell must be highly heat resistant and are therefore made out of tantalum. To the outside, heat radiation is controlled by a water cooling system, that provides very effective shielding of heat, eliminating the need for additional provisions for the 2D MOT chamber or other structures surrounding the oven. One should at this point note, that even though the exterior design remained relatively constant, the interior design, i.e. the arrangement of the collimating apertures, the radius of the opening at the tip etc. were, over the course of the development of the oven, significantly changed compared to the initial offer of the manufacturer. This work was done by Lauriane Chomaz and Jianshun Gao in coorperation with the company.

The effusion cell with the surrounding cooling tube will be mounted on a CF40 flange. On the other side of the flange are connections for water supply and control. To improve the capturing process, it is generally favourable to have the beam source as close to the capture region as possible, in our case to the centre of the chamber. But also, the oven must not interfere with the laser beams for cooling in any way, otherwise random laser reflections could occur, which we do not want. The tip of the oven aperture has a diameter of 25 mm, the laser beam diameter still needs to be determined precisely but will be smaller than 38 mm. At this maximum beam diameter the minimal distance from the chamber centre to the oven is approximately 39.37 mm. We decided to mount the oven tip 40 mm away from the centre. This should be achieved in the following manner: the oven is overall 420 mm long, 75 mm extend into the chamber, while a 345 mm long tube with flange connections on both sides will connects the oven's own flange to the oven flange of the chamber (see Figure 5). According to the manufacturer of the oven, the inner diameter of the tube and the chamber drilling hosting the oven should be at least 40.5 mm in diameter, even though its maximum outer diameter is 38 mm. The oven as well as the connection tube will be realized by *CreaTec Fischer & Co. GmbH.*

3.2 2D MOT chamber

After exiting the oven, the atoms reach the 2D MOT chamber. The 2D MOT chamber was designed to fulfill a few simple requirements while still being as compact as possible. One of the first essential questions regarding the chamber is whether it should be carved out of a solid block

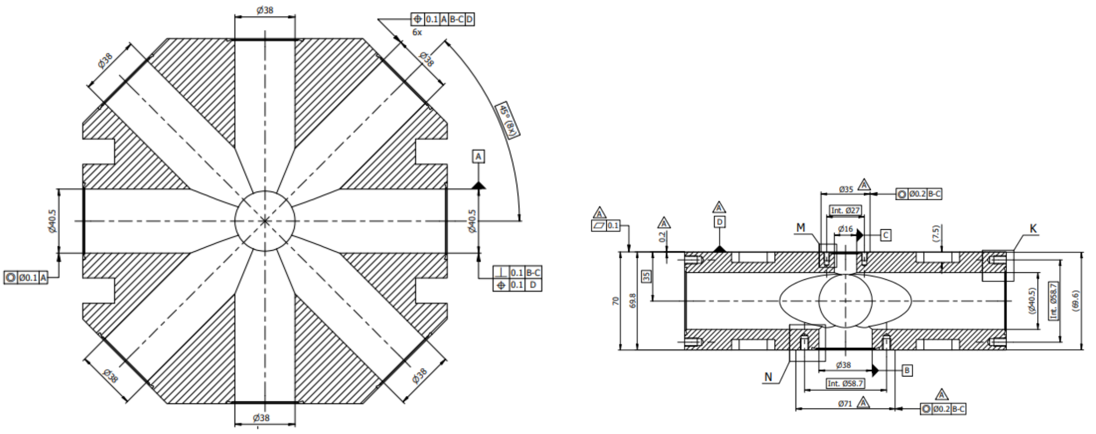

Figure 6: Mechanical drawings of the 2D-MOT chamber provided by *SAES Vacuum Technology*. On the left a view on a cross section of the octagon with all drillings for the oven and laser beams. On the right a side view with the flange connections for the pumping stage as well as the differential pumping stage and the extrusions for the permanent magnets.

or welded together from multiple parts. Both groups at Heidelberg are using the same 2D MOT chamber (see Figure 7), which is carved out of a solid block and extremely compact[14] [13]. That chamber is in fact so compact that despite its octagonal shape, it is not possible to attach CF40 flanges to all eight sides, which is not necessary for these experiments because the atomic beam sources for alkali metals are very small compared to our dysprosium oven and can be connected to the chamber via a CF16 flange. However, to host our oven and cooling beams, the chamber should have CF40 connections on all sides. In many of the slightly more historical references (which in this context means, experiments older than about seven or eight years), the chambers consisted of a set of tubes, spanning a two-dimensional plane, which were welded together, so to see for example in [6] or [26], the latter experiment as well as [8] even using glass cells as 2D MOT chambers as well. We decided not to have welded parts on or near the chamber, since machining a part from a solid metal block usually provides better precision in the alignment of the beam paths and better vacuum quality. All that is crucial, especially when designing something never done before, namely a 2D MOT with dysprosium atoms. Also welding could potentially change the magnetic properties of the material and thus disturb the magnetic field of the MOT.
In total requirements for the chamber include eight CF40 flange, four for cooling beams, two for imaging beams, one to connect the oven and one that could potentially host a Zeeman slower at a later stage. In addition, the chamber should be carved out of a solid block of non-magnetic material with the flange connections far enough from the centre so that the atomic beam source can be inserted into the chamber with the output close to the centre and the beam cone not touching any viewports on the opposite side. The now following section is a detailed description of the custom design of our 2D MOT chamber.

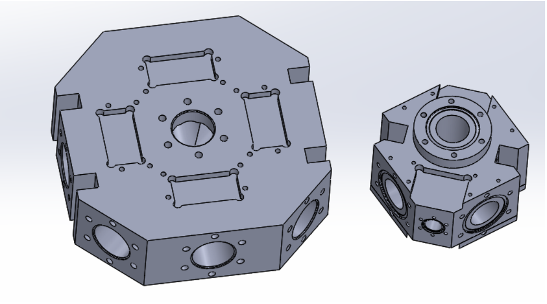

Figure 7: Size comparison between the chamber used in the two other groups at Heidelberg (right) and our custom design (left)

The shape of our chamber follows that of an octagon with an inner diameter of 250 mm. This gives us eight side surfaces, each with a length of 103.6 mm. This structure was chosen to ensure that one can directly fit CF40 viewports on said side surfaces, without any external tube structure and also to make sure that one can use the proposed adapters (*VFA275/M*) from *Thorlabs* for optical cage structures around two adjacent viewports without them interfering in any way. The depth of the chamber in transverse direction is 70 mm, such that there is just enough space for CF40 standard flange connections on the side surfaces. From the regular octagon two opposing sides as well as the two opposing sides on the orthogonal axis are slightly skimmed by 10 mm. This is solely done to save space and material, and thus weight. From now on, the axes on which the sides have been skimmed out will be referred to as the x-axis and the y-axis, with the x-axis horizontal and the y-axis vertical in the final assembly. The direction of the push-beam transversely through the chamber will be referred to as the z-axis.

The different flange connections serve different purposes. On one side along the x-axis is the connection for the oven and on the opposite side a blind flange, since the atomic beam of dysprosium atoms would hit a viewport there and likely stick on it, quickly producing a dysprosium coating on the inside of that viewport, which would then be unusable for optical access. The drilling on the x-axis will be through the whole diameter of the chamber, just as on every other side-to-side axis in the x-y-plane, but with a diameter of 40.5 mm in order to host the oven, whereas every other drilling has a diameter of 38 mm to host laser beams. The flange connections on the y-axis may be used for imaging or even connecting a Zeeman-slower at a later stage. The four remaining viewports on the diagonal axes in the x-y-plane are used for the cooling beams. On the z-axis a CF40 flange connection is situated on one side to connect the pumping stage and the input of the push beam, on the other side a CF16 flange connection for the differential pumping stage. The drilling for the CF40 flange has a diameter of 38 mm and the one for the CF16 flange has a diameter of 16 mm.

In addition to the flanges on the two opposing large surfaces parallel to the x-y plane, there are a total eight small extrusions, two on each side, in which the permanent magnets are put to generate the magnetic quadrupole field required for the spatial confinement in the 2D-MOT (see 2.5). The extrusions are placed along the x and y axes and have a rectangular shape with a size of 31*60 mm, with the shorter side parallel to the respective axis on which they are arranged. The longer edge has a normal distance to the chamber centre of 63 mm. This was chosen in accordance with the simulations of the magnetic field produced by the magnets at different positions (see 5). The

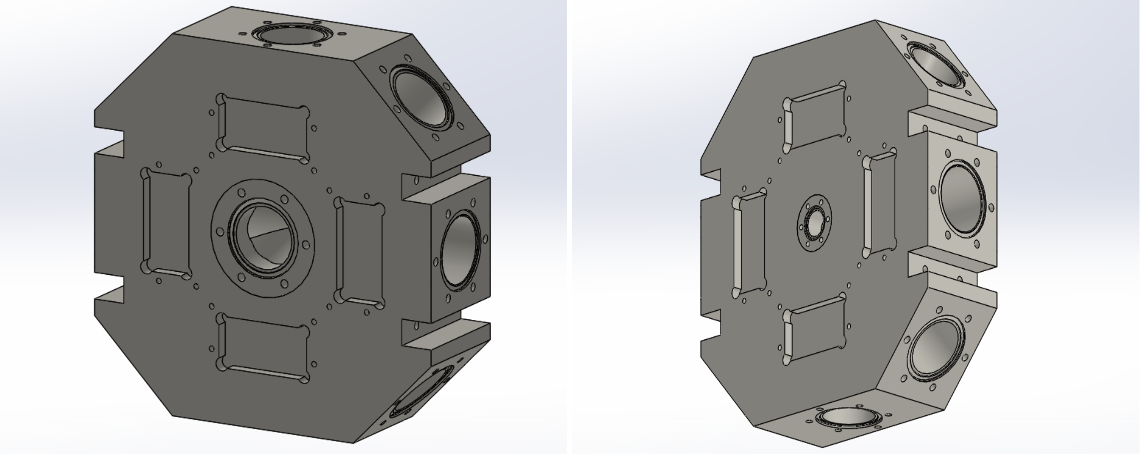

Figure 8: Pictures of a 3D model of the chamber provided by SAES Rial Vacuum. On the left a view on the large surface with the CF40 connection for the pumping stage. On the left a view on the CF16 connection for the differential pumping stage.

extrusions are 7.5 mm deep. The idea behind this is that since the magnets being 10 mm high, they do not completely fit into the gaps provided for them, but are held and fixed by a specially made plate, that is screwed on top.
Finally, on the side surfaces that are orthogonal to the axis, four small extrusions to mount the chamber are made. Two on each side, one above and one below the flange connection for the oven. The extrusions are each 16 mm high and 20 mm deep and extend over the entire 70 mm of the side surface. All dimensions of the chamber as well as the standards of the threads for all screws are metric. To reduce outgassing of hydrogen and ensure a good vacuum quality until at least 10^{-12} mbar, the chamber will be made out of a solid titanium block. The custom design we have worked out will be realized by *SAES Rial Vacuum* in Parma, Italy. According to their calculations the overall weight of the chamber will be 9.529 kg.

3.2.1 Magnetholders

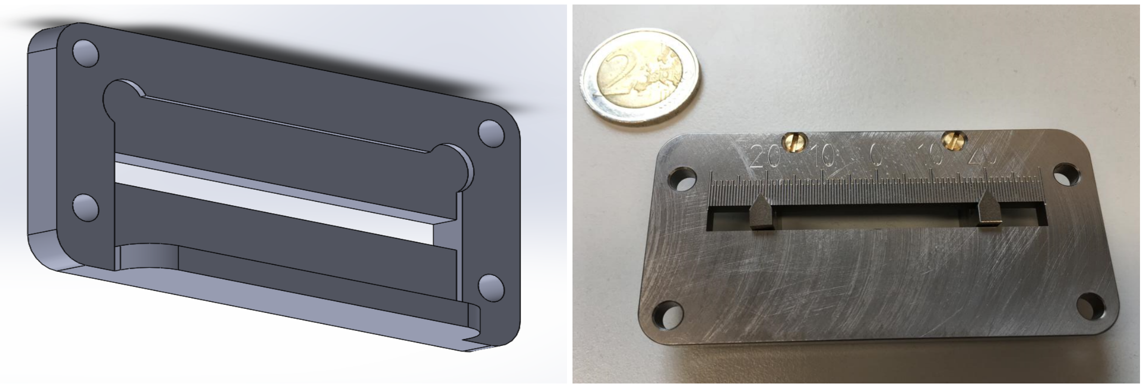

Figure 9: On the left a 3D model of a holder plate, view on the inside. On the right a top view on the same plate with a millimeter scale engraved on top, manufactured by the mechanical workshop out of titanium.

As mentioned in the section before, the permanent magnets are placed in small extrusions on the 2D-MOT chamber and held in place by some custom designed magnet holder plates. The magnets themselves look like little plates and have the dimensions 25*10*3 mm. The magnetic moment lies normal to the large side of the magnet. Since we need the magnetic moment to be orthogonal to the x and y-axes, the extrusion with a width of 60 mm allows for a maximum number of 20 magnets. But since we plan to build some handlebars in addition to the magnet holder, with which one can easily move the magnet block slightly to the desired position, it will actually not be possible to accommodate more than 17 magnets in one extrusion. As one can see in Figure 8, the extrusions have a little circular shape in each corner. The reason for this is purely a manufacturing issue. Since the milling machine used to drill the extrusions has a circular head, these little circular corners must be made to ensure, that the full height and width of the extrusion can be used. The same applies for the holder plates, which are 5 mm thick and 40.5*80 mm large. On the inside, so the side facing the chamber surface, there is a 1 mm deep extrusion, that fits directly on top of the extrusion on the chamber, except that on one side of said extrusion there is a 6 mm high extension perpendicular to the plate to hold the magnets in place. With this additional extension in place the space for the magnets reduces to 26 mm in height, which means they only have 1 mm of room to spare. In the center of the plate there is a 60 mm long and 5 mm wide notch into which the handles are inserted and which can be accessed if necessary to hold them in place during construction. With a scale engraved on top of the magnet holders, the handles can also serve as indicators, since the position of the magnets is directly influencing the position of the capture region inside the chamber. It is planned to have the holder plates as well as the handles made out of titanium and manufactured by the mechanical workshop of the physics department.

3.3 Other custom vacuum parts

The main requirements for vacuum parts are a low outgassing rate, corrosion and high temperature resistance, and the lowest possible magnetization, which should not change during a heating process. Materials fulfilling these requirements are titanium, stainless steel or aluminium. Aluminium is less heat resistant than the other two. Stainless steel has the highest outgassing rate due to the production process, where it is impossible to exclude the possibility of hydrogen being trapped in the material. For reducing the outgassing rate, a common procedure is to heat the whole vacuum assembly up to more than 100°C for more than a day to get rid of the hydrogen inside the material. Stainless steel also comes in different variations concerning the exact composition. While AISI 304 steel is more common and cheaper, AISI 316 LN and AISI 316 L [22] have better magnetic properties for our experiment, which is why we decided to have everything in close proximity to the MOT chambers made out of one of the latter non-magnetic steels. For the whole assembly, three other custom vacuum parts were designed, apart from the 2D MOT chamber. They are all made of AISI 316 LN or L stainless steel respectively and manufactured by *SAES Rial Vacuum*.

3.3.1 Pushing and pumping stage

As can be seen in Figure 4, there is a tube arrangement on one side of the 2D MOT chamber, which we refer to as the pumping and pushing stage, since it serves these two purposes. It is connected to the chamber through the CF40 flange on the z-axis. The shape is relatively unusual, due to multiple requirements on this custom part. Firstly it should have a connection for the Ion-Getter pump, used to produce the high vacuum. But since the getter pump can not be activated at the normal environment pressure, there must also be a connection for a so called pre-pump to bring the pressure to a level at which the main pump can be activated. Secondly we would like to know how high (or hopefully low) the pressure is in the chamber itself and therefore need a connection for a vacuum gauge. And thirdly we need an input for the push beam along the z-axis, which means a viewport.

Said push beam is the main reason why the pushing stage has a somewhat odd shape. On the

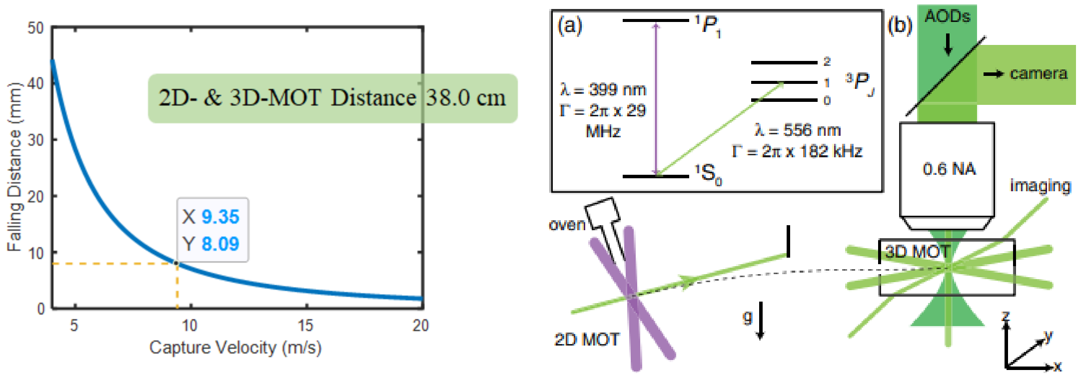

Figure 10: On the right, a sketch of the falling distance of atoms over the MOT to MOT distance, done by Jianshun Gao. On the left a sketch of the 2D and 3D MOT arrangement of the ytterbium experiment in the group of Jeff Thompson at Princeton university. See also [25].

2D MOT we had a CF40 flange connection, so that there is enough room to have the extrusion for the permanent magnets. However during the simulation of the particle trajectory from the 2D to the 3D MOT with a horizontal push beam along the z-axis, we realized that the atoms fell out of the capture region by the time they reached the main chamber, due to gravity. The problem is in fact that since the atoms are pushed below the capture velocity of the 3D MOT, their time of flight from one MOT to the next is too long, so that they fall due to gravity. This problem was not encountered by any of the other groups in Heidelberg, partly due to the much lighter atom species, but mainly because the transitions the respective atom species used in the 3D MOTs allow for a higher capture velocity, thus a higher transport velocity between the traps, shorter time of flight and less falling distance. But since the narrow dysprosium transition in our 3D MOT leads to a relatively low capture velocity (see Figure 10), we needed to find a solution to compensate the falling. One should also note, that a low velocity of the atoms also increases the divergence of the atomic beam. We are thus only even more interested in keeping the transport velocity between the MOTs as low as necessary but as high as possible.

One option to compensate for the falling would be to tilt the whole 2D MOT chamber by a small angle, such that the atoms will be sort of 'tossed' out of the chamber and 'land' in the main chamber. We know that the group of Jeff Thompson at Princeton built such a contraption for their experiment with ytterbium [25], because they are also working with heavy atoms and in fact encountered the same problem regarding the narrow 3D MOT transition as we did (see Figure 10). To have a tilted setup would however require very precise machining of all vacuum parts and mounting, since maintaining the right angle is crucial. Since for our setup only a very small tilting angle would be sufficient, we decided not to tilt the whole chamber, but only slightly the push beam, such that the input would have a small offset from the z-axis, but then cross the centre of the 2D MOT chamber and is ultimately blocked and does not reach the main chamber. To make sure, that the input can host the push beam also with a slightly larger offset than calculated and with its full beam waist, it was necessary to have a CF63 viewport at the input.

The pushing and pumping stage (Figure 11) is therefore connected to the 2D MOT chamber via a CF40 flange followed by a tube along the z-axis with an inner diameter of 39.2 mm. This CF40 tube is only 30 mm long before it transitions into a 92.2 mm long tube with an inner diameter of 66 mm. The CF63 flange connection is then located at the end of this tube. Thus the total length along the z-axis of this part is 152.2 mm. In one of the earlier design drawings, the transition between CF40 and CF63 was realized by a cone shaped tube with a fixed half angle between five and ten degrees. However, *SAES* suggested the solution described above, since it is easier to machine especially concerning the welded parts, and even offers a better flow conductance of particles contaminating the vacuum towards the pump. The pump itself is located on top of a 66 mm wide tube that extends straight up along the y-axis. It is mounted on the previously mentioned CF63 tube and is 182 mm long. A CF40 flange connection for the vacuum pump is located on the. Located 62 mm below the top, two more CF40 tubes with flange connection perpendicular to each other are placed. One facing in x-direction, the other one in z-direction. These are used to connect a vacuum gauge and a pre-pumping stage. This stage will be connected through a valve, so that it can easily be mounted and dismounted without breaking the vacuum. The whole part is produced out of multiple tube parts, all made out of 316L stainless steel, and is welded together using the TIG method (see [4]). According to *SAES*, the welding will cause no excess material on the inside and will also not change the magnetic properties up to a significant extent.

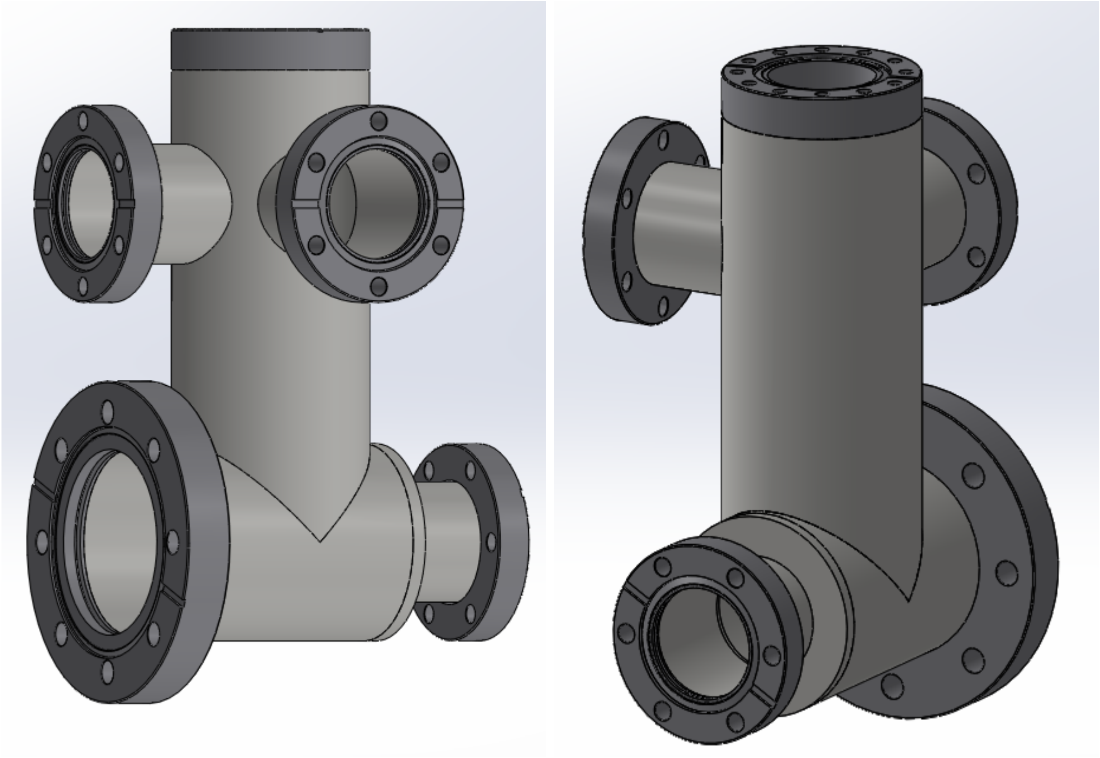

Figure 11: 3D model of the pumping and pushing stage provided by SAES Rial Vacuum

3.3.2 Differential pumping stage

To separate the high vacuum from the ultra high vacuum part, we need a differential pumping stage. As in all other referenced experiments so far, the stage is meant to filter particle trajectories on one side, but also let the collimated atomic beam pass. Since in the latter part we are planning to reduce the pressure down to around 10^{-12} mbar, there is no way around a separation that divides the rather large in which the high vacuum is to be established from the ultra high vacuum part. The main source of contamination will likely be the oven region, but the smaller volume on the ultra high vacuum side can be pumped more efficiently and with its own separate pumping stage. The pressure difference that can be maintained is directly related to the exact dimensions of the pumping stage. Exactly how the flow conductance changes as the dimensions change and why we chose this design for our setup is discussed in more detail in 4.6, while the following section deals with the mechanical design that results from these considerations.

The differential pumping stage (DPS) is connected to the CF16 flange of the 2D MOT chamber along the z-axis. In principle it is nothing else than a very narrow tube. In our case it is in fact a little cone-shaped tube with a half angle of 2° in order to also host the divergence of the atomic beam. The divergence is actually smaller than 20 mrad (ca. 1.1°) but since the vacuum conditions allowed so, we rounded the cone's half angle up generously to 2°. The cone has a length of 55.7 mm and the initial radius is 1 mm. This means that the radius at the end of the cone is just a little below 3 mm. The cone will be carved out of a cylindrical block with a total length of 57 mm. There are two flange connections on the cylinder, which separate it into two parts (see Figure 12). The first part is 16 mm long and has a diameter of 15 mm. It will be pushed into the 2D MOT chamber and fixed through the first CF16 flange connection onto the large surface of the 2D MOT octagon opposite from the push beam input. The length of the first section is chosen so that the opening of the DPS is as close as possible to the centre of the 2D MOT, so that dysprosium atoms

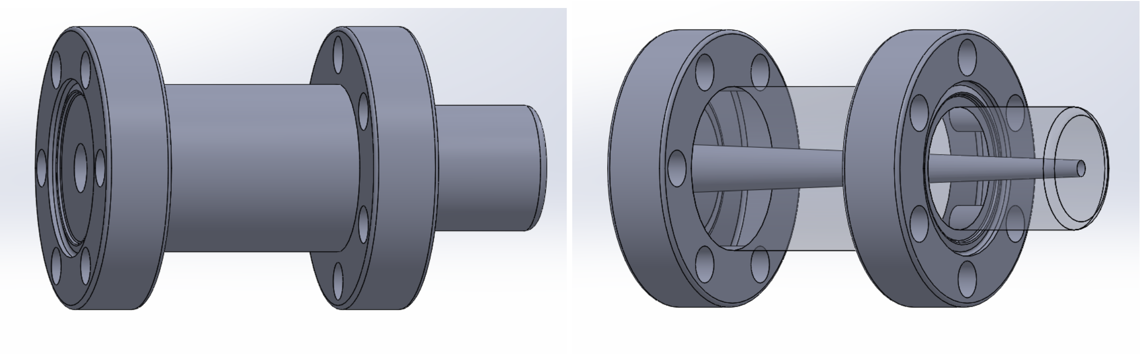

Figure 12: On the left a 3D model of the DPS. On the right the same model with transparent surfaces, so that the cone-shaped tube on the inside becomes visible.

can be efficiently pushed towards the 3D MOT, but as far away from the centre as necessary so that it does not interfere with the cooling beams and cause uncontrolled laser light reflections.
The second part between the two flanges has a radius of 20 mm and is 25 mm long for the sole reason that this length is sufficient to insert the screws for tightening the two flanges when assembling the entire device. The second CF16 flange is connected to a gate valve that serves only as a shutter, which in addition to the DPS also offers the possibility of completely sealing one vacuum section while the vacuum in the other section must be broken, e.g. when the oven must be removed and refilled.

3.3.3 Connector box

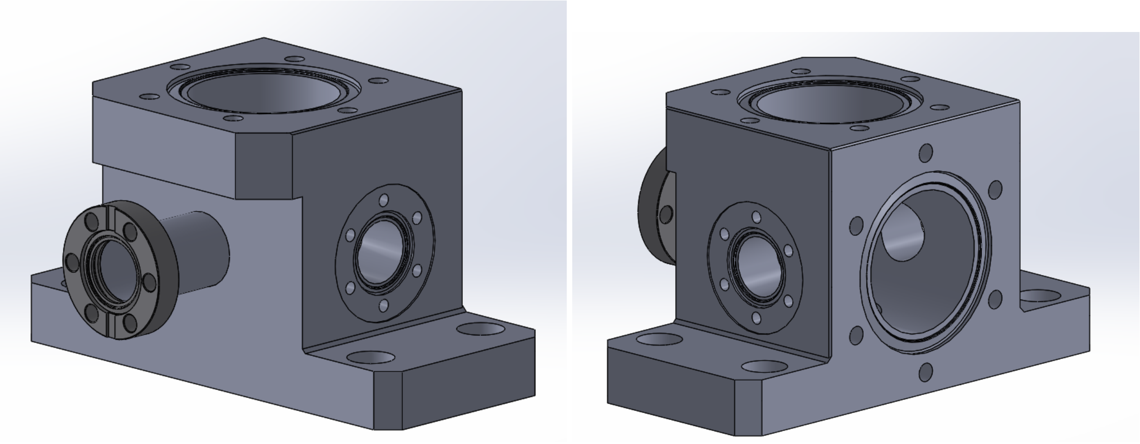

Figure 13: 3D model of the connector, on the left with the small tube connection towards the gate valve in the foreground, on the right the CF40 flange to connect the main chamber.

The last obstacle, that the atoms have to pass on their way to the main chamber is a small connector box. The design is adapted from the HQA [13] with some minor changes. The box serves multiple purposes. Perhaps the most important purpose is that the pumping stage for the ultra-high vacuum section is be connected above it. But due to its cubic design it serves as the main point of support when mounting the whole experiment. The main change from the HQA is that additional CF16 viewports have been added on three sides to improve the optical access.
The connector box is connected to the other side of the gate valve mentioned above. From the CF16 connection, a small tube with a length of 32.2 mm connects along the z-axis to the box itself (see Figure 13). The tube is welded perpendicularly onto the surface of the box. The box is carved

out of a solid block of stainless steel and has a base with the shape of a 118*56.5 mm rectangle and a height of 15 mm. This base serves as a connection to a solid mount that is screwed onto an optical table and connected to the box via four screws. The relatively large surface that connects the base to the mount is supposed to provide a stable and well aligned point of support for the whole vacuum system. However, in the middle of the base's surface, a CF16 viewport is located to be used for imaging.

The box itself is mounted onto the base and resembles a cubic shape with the dimensions 70*57*56.5 mm. Two additional CF16 viewports will be added to the two side faces that are perpendicular to the x-axis to improve optical access and potentially provide additional slowing beams. On top of the box the pumping stage of the ultra high vacuum section will be connected through a CF40 flange. In order to have enough space to mount a CF40 connection on the top, a slight overhanging part to fix the screws is necessary, such that the top surface is a square with side lengths 70 mm. Ultimately the connector box has another CF40 flange on the side opposite of the small tube connection to attach a short CF40 tube, which connects to the main chamber. The main chamber has a commercial design, at least during the first intermediate time stage of the experiment

3.4 Assembly and Mounting

Finally, all the parts are designed to form a setup, which is of course considerably larger than the setups of the groups working with alkaline atoms, but yet comparably small. The full vacuum setup will fit inside one cubic metre. As mentioned before, the connector box is mounted on two custom made aluminium blocks that serve as the main point of support. Since the connector has a large bottom surface, which is then screwed on top of the mount, we plan to achieve a high level of parallelism between the main axis of the experiment (the z-axis) and the surface of the optical table on which the mount is fixed. Once the box is tightened, all other parts of the assembly are connected to this fixed point and along the horizontal axis. Due to the weight of the 2D MOT chamber, it will itself require a support to prevent excessive mechanical stress on the system. The mount used here is supposed to support the chamber vertically, so that the setup is not stretched or squeezed along the horizontal axis. When this mount is tightened to the chamber, the screw holes are not in the exact positions, but have a loose oval shape. Finally, the pumping and pushing stage as well as the oven are each supported by a similar structure. Since both have a circular shape, it is of little use to calculate an exact height that a mount would need to have in order to align these parts along the main axis of the experiment. Rather, we will build a height-adjustable mount consisting of a large screw connected to a clamp, that attaches around the oven and the pushing stages flange. This screw will when turned either push the clamp up or lower it down, such that one can adjust the height of the mount by hand to the right size. This solution has already been tested in Paris in a cold atom experiment on strongly interacting Fermi gases [17] .

In order to guarantee a sufficient vacuum, it is necessary to ensure that the entire apparatus is tightly sealed, which is usually done with copper gaskets. Each flange connection has a knife edge that goes in a full circle around the opening. When one flange is connected to the next, a ring-shaped copper gasket is inserted in between them. The knife edges of both flanges then cut into the softer copper when the connection is screwed tight. Therewith a full metal transition is established and the connection is sealed for high and ultra high vacuum. However, since the knife edge cuts into the material of the gasket, they can only be used once and need to be replaced once the flange connection is unscrewed. The material used to make the gaskets can vary depending on the heat resistance, the chemical reactivity and the vacuum quality required. In general copper is the most widely used material, but if during the operation of the experiment or the bake-out process temperatures rise higher than around 600°C the stability of copper may decrease and even though one is far away from the melting point, it may cause leaks which lead to a rapid increase of pressure. That is why nickel is a common alternative for experiments involving high temperatures. It is also common to coat a copper gasket with a less reactive material such as silver or even gold to assure that chemical reactions between the atom species used in the experiment and the gaskets do not lead to leaks over a longer period of time. In the alkaline mixtures experiment of Fred Jendrzejewski for example nickel and silver plated gaskets are used. Concerning our experiment, there is only one source of heat, which is the atomic beam source. Even though temperatures above 1000°C are required in the effusion cell of the oven, it is surrounded by a water cooling setup, which has been proven to be very effective in previous experiments. Also, in the tests conducted by the manufacturing company concerning the heat radiation from the oven tip, the temperature decreased rapidly within 20 mm. We therefore conclude that no special heat-resistant material is required, and since we are not dealing with highly reactive alkali metals, no protective coating is necessary. The gaskets are made of oxygen-free high-conducting copper and annealed to ensure sufficiently low pressures also in the ultra-high vacuum regime. They are standardized for CF16,40,63 and 100 flange connections and are ordered from *Hositrad Vacuum Technology* in Hoevelaken, Netherlands.

4 Vacuum

In our experimental setup we want to cool atoms down to temperatures in the nK region. If atoms collide with other particles they always transfer kinetic energy, and accelerate or heat up. In order to prevent this, we need to increase the mean free path of the atoms, which depends only on the geometry of the atoms and the particle density n. Having no influence on the atoms geometry, we need to decrease the particle density, or in other words decrease the pressure. As already mentioned in section 3, the experiment will be divided into two parts, the high vacuum part and the ultra high vacuum part. As the name suggests, the only difference between those parts is the pressure. In the high vacuum part consisting of the 2D-MOT, the pumping stage and the oven apparatus, we are aiming for a pressure of approximately 10^{-8} mbar. In the ultra high vacuum part, which is separated from the rest of the experiment through the differential pumping stage, we want to reach a pressure of 10^{-11} up to potentially 10^{-12} mbar.

As can be seen in Figure 14, with the pressures we aim at, we are well within the free molecular flow regime. This means for simulating the particle flow and therewith the vacuum in the chamber, it is fair for us to assume no particle-particle collisions, but free molecular flow instead. One can also see that different pumps are needed for different vacuum qualities. However, the following calculations are only concerned with the setup already being in operation, so assuming all leaks are detected and fixed and a sufficiently high pressure to start the Ion-Getter pump is already reached. When first establishing the vacuum, the Ion-Getter pumps can not be used from the beginning, one rather has to start pumping with a regular scroll pump and later with a Turbo Molecular pump. During this pumping process, leaks will most likely become detectable as the pressure may eventually stop to decrease further due to a leak. In order to find leaks one can go through a common leak testing process, during which one sprays a little helium on a potential leak spot. If thereafter the pressure in the chamber increases significantly, the leak is found. In our case we also plan to attach a residual gas analyser (RGA) to the pumping stage which can give even more detailed information about the gas composition on the inside of the chamber. Most likely leaks will occur at the CF flange connections. To seal the connections, standard vacuum annealed copper gaskets are used. These gaskets are inserted between two flange connections and the knife

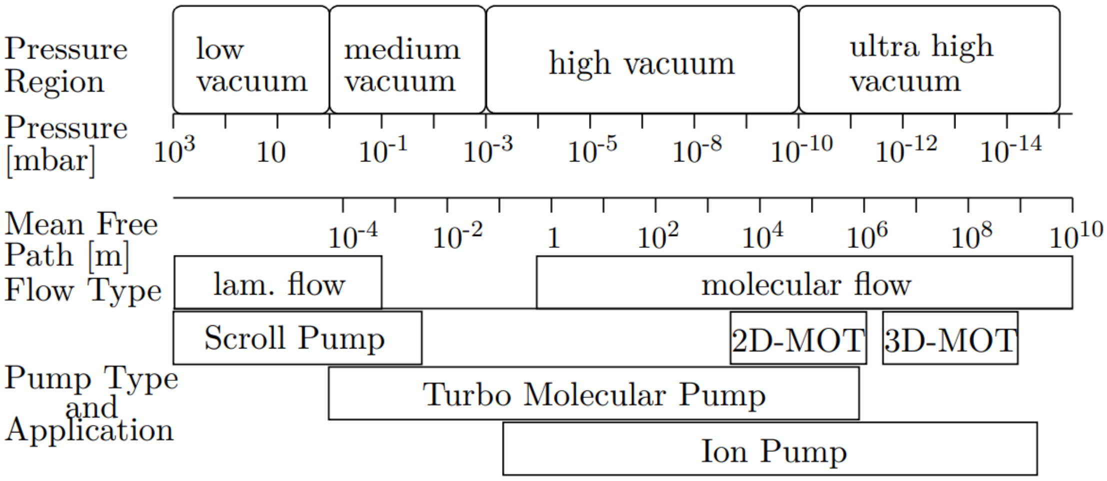

Figure 14: An overview over the different vacuum regions with the mean free path and the pumps used in the respective regions and our apparatus chambers. Figure adapted from [11]

edge of each connection will cut into the softer copper a little such that the connection is sealed. The gaskets are made of oxygen free copper with a high conductance. In order to seal the flanges also for our low pressure regime, they have to be vacuum annealed and should be stable until at least 450°C.

In the now following sections, the results of some calculation and simulation results will be presented. These calculations and simulations were conducted in order to get a rough idea of what the vacuum quality for our custom built apparatus may turn out to be.

4.1 Molecular flow theory

We assume free molecular flow, so particles only interact with the walls of the vacuum tubes and chambers of our apparatus and not with each other and their velocities are distributed according to the Maxwell-Boltzmann distribution, whose mean value is $\bar{v}$. The velocity of a single particle is assumed to remain constant except when a collision with one of the walls occurs.

$$\bar{v} = \sqrt{8\frac{k_B T}{\pi m}} \tag{4.24}$$

Here m is the mass of the particle. We can assume that once the vacuum is established sufficiently and the operation can begin, the main source of contamination will be residual substances enclosed in the the enriched dysprosium inside the oven and especially H_2 outgassing from oven region, especially due to the high temperatures required in the oven. There will also be some outgassing from other vacuum parts (see [3]). But since we plan to have all vacuum parts manufactured either from high quality stainless steel or titanium, the outgassing rate will most likely be very small, especially after baking. Thus we assume H_2 from the oven area to be the main source of contamination. In order to get a rough estimate which pressures we can reach with our pumps, and to test via simulations whether the differential pumping stage works in the desired way, we will calculate the flow conductances of the different vacuum parts and thus simulate the particle flow from the contamination source to the pump piece by piece. In general the flow conductance C of a vacuum component can be calculated in the following manner [18]:

$$C = \frac{\bar{v}}{4} A P \tag{4.25}$$

with the A being the cross section of the entrance of the element and P being the passing probability. While A can usually be precisely measured and in most cases is standardized, one can not always calculate P analytically. There are very precise formulas for some standard pieces such as tubes or T-pieces, but especially for custom parts it is often the easiest way to simulate the particle flow through a vacuum part and calculate the passing probability numerically. Once the flow conductance has been calculated for all necessary vacuum pieces, the serial connection formula provides a way to calculate the conductance of the whole way from the source of contamination to the chamber [18].

$$(\frac{1}{C_{tot}} - \frac{4}{\bar{v}A}) = \sum_{i=1}^{N}(\frac{1}{C_i} - \frac{4}{\bar{v}A_i}) + \frac{4}{\bar{v}}\sum_{i=1}^{N-1}(\frac{1}{A_{i+1}} - \frac{1}{A_i})\delta_{i,i+1} \tag{4.26}$$

with

$$\delta_{i,i+1} = \begin{cases} 1 & \text{if} \quad A_{i+1} < A_i \\ 0 & \text{if} \quad A_{i+1} \geq A_i \end{cases} \tag{4.27}$$

The last part of the flow connection formula (4.26) is only non-zero if the cross section A becomes smaller for two adjacent parts. If a pump is connected to the vacuum structure, the pump can be regarded as an element with perfect vacuum, so pressure p and particle number density n both equal zero. The total flow conductance, so all flow conductances of the separate pieces, combined in the way (4.26) dictates, can then be seen as the effective pumping speed of the pump S_{eff}. The pumping speed S that the manufacturer specifies for the pump will as well be included in the flow connection formula. What we have to estimate is the contamination output from the beam source q_N. After that we can calculate the particle density in the initial vacuum part.

$$C = \frac{q_N}{n_1 - n_2} \tag{4.28}$$

Here n_1 can be seen as the particle number density in the initial chamber, in our case the 2D MOT chamber, and n_2 can be set to zero, since it applies to the vacuum pump. The particle density is directly related to the pressure via the ideal gas equation.

$$p = nk_BT \tag{4.29}$$

4.2 Vacuum pumps

There is a variety of different vacuum pumps, designated for different vacuum regions (see Figure 14). Operating a vacuum pump in the wrong region will in the best case be only very ineffective but may in the worst case damage the pump. When establishing the high and ultra high vacuum in our experimental setup, in total three different pumps will be necessary. What is most important here is that the more sensitive pumps are not turned on too early and that only oil free pumps are used as to not cause any unnecessary contamination inside or outside the chamber.

4.2.1 Prepumping

The first pump used to bring the pressure down from atmospheric pressure is a regular oil-free scroller pump. Although the exact arrangement may differ from pump to pump, the way it operates is usually very similar. Air is trapped and compressed by two counterrotating spirals, it is then pushed towards the exhaust, where it is pumped. During the first part of the cycle the empty volume between the spirals will suck in air from the chamber, once the spirals have rotated far

Gas	NEG activated [l/s]	NEG saturated [l/s]
H_2	290	6
H_2O	180	4
CO	140	5
N_2	80	4
CH_4	15	15
Ar	6	6

Table 3: Pumping speeds of the *NexTorr Z200* Ion-Getter pump from *SAES Rial Vacuum*, given for different air molecules [12]

enough that the air has been transported away from the pumps opening, it is trapped. The air is then further compressed and transported towards the exit of the pumping chamber. Depending on the size and exact layout of the scroller pump, multiple cycles can be performed at the same time so that the vacuum part is continuously pumped.

As can be seen in Figure 14, a scroller pump can only reduce the pressure a little below atmospheric pressure. For further pumping a so-called Turbo Molecular pump (TMP) will be started. For this pump it is already relevant that the mean free path of the air molecules is sufficiently larger than at atmospheric pressure, so that only collisions with the walls of the pumping structures are relevant and collisions among the molecules are reduced. The general idea of the TMP is to manipulate the molecules' trajectory by rotors that are pushing them towards the exhaust of the pump once a molecule hits the wall of a rotor blade. The blades are oriented to transfer momentum toward the exhaust onto the molecule upon impact, and this process continues through multiple rotors while the molecules are also decelerated and compressed by non-rotating rotors. The TMP can operate well into the high vacuum region, but to reach ultra-high vacuum and to maintain it over a long period of time, yet another pump is necessary.

4.2.2 Ion-Getter pumps

As the name suggests, Ion-Getter pumps consist of two parts that are yet functioning in a similar way. The conceptual difference of the Ion-Getter pump in contrast to the other pumps is, that molecules are not pushed towards an exhaust but rather are chemically bound to the surfaces of the elements. The getter element consists of getter surfaces reaching into the vacuum chamber. If so-called active gases such as hydrogen, nitrogen or also carbon dioxide hit these surfaces, they will be dissolved into their components which then diffuse into the material of the element. If this process is continuously occurring over a long period of time, the getter element will be at some point saturated such that it can no longer bind molecules and pump the vacuum chamber efficiently. Then it needs to be reactivated, which mainly means it is being heated to a point, that the hydrogen on the surface recombines. Those gases that remain unaffected by the getter elements will simply pass them and reach the Ion element. Inside of this element, there is a strong magnetic and electric field. In such fields, free electrons are heavily attracted to the positive anode while at the same time being trapped in a circular movement due to the Lorentz force caused by the magnetic and electric field together, and are thus spiraling through the element. Via collisions with these spiraling electrons, non-active gases entering the element, such as argon or other noble gases but also methane, will be ionized and thus pulled towards the negative cathode where they are likewise bound chemically just as in the getter element.

The table above (see Table 3) gives an overview of the pumping speeds, that can be achieved for different gases and also pictures the rapid decrease in pumping efficiency once the getter element is saturated. In our experimental setup, we will have the same Ion-Getter pump once for the high-vacuum section and once for the ultra-high vacuum section. Following the choice of many modern cold atom experiments, especially at Heidelberg, we decided on two *NexTorr Z200* pumps from *SAES Vacuum Technology* each with a pumping speed of 290 l/s for H_2. The Z generation is a renewed and optimized line of Ion-Getter pumps by *SAES*, which makes it naturally preferable over the older models. The *NexTorr Z200* pump specifically suits our vacuum requirements well (see also 4.5) . It is very compact, weighs only 2.2 kg and can be attached to the vacuum apparatus via a CF40 flange. From those pumps that have a CF40 connection, this one provides the highest pumping speeds.

4.3 Vacuum simulations

This and the following two sections will be concerned with the method we used to get a rough estimation of the vacuum quality in our chambers. It should be noted that the results are by no means based on exact calculations, but rather on a series of approximations involving the particle flow as well as the geometry of the chambers. During all calculations free molecular flow was assumed and collisions among particles neglected.

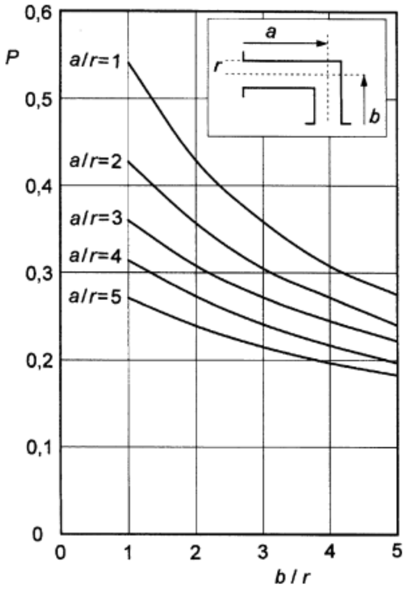

Figure 15: Passing probability of an elbow piece with arbitrary for arbitrary dimensions. Figure taken from [18]

As described in part 4.1, the main objective is to calculate the conductance of the various vacuum pieces through which contaminating particles have to flow to reach the pumps and to be extracted from the system. In order to calculate the conductance of the pieces, one does not only need to know their geometry but also the probability with which a particle passes this piece (4.25). While this probability can be precisely calculated for some standard vacuum pieces such as tubes or right angle elbow pieces, it may differ for custom pieces. The probability is therefore also simulated. The simulation works through a *Python* script that calculates the trajectories of particles in three-dimensional space. At the start a particle is set at a random position within the input cross section of the vacuum piece. It has a random input angle. The velocity amplitude is not really relevant for the simulations themselves, since these only compute the passing probability, which is independent of the absolute velocity. The simulation therefore works only with a step distance and a velocity vector with that exact length. The script then calculates the new position of the particle with every step as it flows through the piece according to $\mathbf{s'} = \mathbf{s} + \mathbf{v}t$. The step distance is chosen in order to give a reliable picture of the trajectory, but also reduce computation time. Once the position reaches a wall, or in case of the script, a coordinate plane, which is defined as a wall, the particle will bounce off the wall under a random angle. This cycle will continue until the particle escapes through either the input or the output cross section (see Figure 16). The quotient of particles flowing through the output over the total number of particles is then the passing probability. For the narrower tube, input and output cross section can be clearly defined at the two ends of the piece. For the wider T-shaped vacuum piece, a particle is counted as pumped once it passed through the cross section of the vertically attached tube. Note the important approximations of this model: It does not take adsorption at the surface into account, but instead assumes immediate desorption in a fully elastic manner. Thus we can assume that with our model, we will overestimate the pressure in our vacuum regions. For simplicity, we approximated circular tubes with rectangular ones in our code. But in order to counter this approximation we used to same cross section area as in reality for the simulated tubes. However, as can be seen below, there will always be a discrepancy between the numerical simulation and the analytical calculation, that can not only be traced back to statistical defects. A small section on such Monte-Carlo techniques in order to numerically simulate particle trajectories can also be found in [23]. Similar vacuum calculations using the technique and simulating particle trajectories in a two-dimensional plane were carried out by Armin Schwierk at HQA.

4.4 High vacuum

In the case of the high vacuum section of the experimental apparatus this means, assuming the oven to be the main source of contamination, the particles will have to flow from the 2D MOT chamber to the pumping and pushing stage and from there up to reach the pump. This way can be divided into two parts: a tube with an inner radius of 19 mm and a tube with an inner radius of 33 mm, to which another tube is connected. For each of the vacuum pieces, that are relevant on the HV side of the experiment, five simulation runs with 10.000 particles per run were conducted. As we see in Table 4, the estimated value for P, according to our simulations, is 46.01%. On the analytical side of things, the passing probability of a circular tube with an arbitrary length l and diameter d can be approximated with a relative error of less than 0.6% (see [18]).

Piece 1	Run 1	Run 2	Run 3	Run 4	Run 5	∅
Pumped [%]	46.71	45.53	46.33	45.67	45.81	46.01
Escaped [%]	53.29	54.47	53.67	54.33	54.19	53.99

Table 4: Simulation results for the first tube. The 'pumped' percentage refers to the amount of particles, which passed through the output of the piece and the 'escaped' percentage is the amount that went back through the input

$$P = \frac{14 + 4\frac{l}{d}}{14 + 18\frac{l}{d} + 3(\frac{l}{d})^2} \tag{4.30}$$

In the case of our CF40 tube with a length of 67 mm and a diameter of 38 mm, this results in a passing probability of $P = 38.23\%$. Since the geometry of this part is pretty much the only one, for which there is a quite reliable analytical way to calculate P, it is a good way to test our simulation. As it turns out, even though we are roughly in the same region with both values, the relative error of the calculations is just short of 17%. Let us keep that in mind as we continue on with the next piece.

The same procedure was carried out for the T-shaped part of the pumping and pushing stage, which has a larger inner diameter. In that case it was assumed that particles would enter the part under a random angle through the cross section of the CF40 tube. If the simulated trajectory of the particle goes back into that tube, the particle will be counted as 'escaped', if it enters the pumping tube, vertically attached, it will be counted as 'pumped'. Again five runs with 10.000 particles each were conducted. Table 5 shows the simulated passing probability of the pumping

Piece 2	Run 1	Run 2	Run 3	Run 4	Run 5	∅
Pumped [%]	68.85	69.19	69.02	68.82	69.16	69.01
Escaped [%]	31.15	30.81	30.98	31.18	30.84	30.99

Table 5: Simulation results for the pumping and pushing stage

and pushing stage ($P = 69.01\%$). This relatively large probability, is mainly due to the small input cross section and the large output cross section. Thus even if we assume a relative error of 17%, as found before, we land in a region between 57-81 %, which is still much larger than the analytically calculated passing probability. Since this is a custom piece, there is no exact formula on how to calculate a theoretical value for the passing probability. One could however approximate the piece as an elbow piece and find a value according to Figure 15. But since this does not take into account that the input cross section is much smaller than the cross section of the piece itself, the theoretical passing probability is much lower than the simulation result. When simulating the particle trajectories, one can see that the pumping and pushing stage almost acts like a separate chamber and once a particle enters, the way out through the wider tube is a lot more likely. The theoretical value for the passing probability for our dimensions turns out to be approximately $P = 37\%$. So even though the two calculated values have not really anything in common due to the reasons given above, we will come back to this value when summarizing all the results.

Now that we have determined the passing probabilities for the two required vacuum pieces, we can apply the series connection formula to calculate the effective pumping speed for the 2D MOT chamber:

$$\frac{1}{S_{eff}} = \frac{1}{C_{p1}} + \frac{1}{C_{p2}} - \frac{8}{\bar{v}A_2} + \frac{1}{S} \tag{4.31}$$

This formula already takes into account that various terms will cancel out, since for example the initial cross section of the whole aperture and the first piece is of course the same. Yet A_2 will not cancel out, since it necessarily appears on the right side of 4.26 and is not compensated on the left side. S in this case is the pumping speed of the Ion-Getter pump for H_2. This is specified by the manufacturing company (see also [12] and Table 3). For the specific model we chose it can be estimated to be up to 300 l/s. The flow conductances can be calculated via 4.25, but since the velocity may vary with the temperature of the particles, which can not be estimated over the entire path, we will see an overview (Figure 19) of the pressure development for different temperatures later. In conclusion one can say that according to our first results, the simulations have as expected sizable uncertainties, but still come in handy when calculating passing probabilities for custom parts.

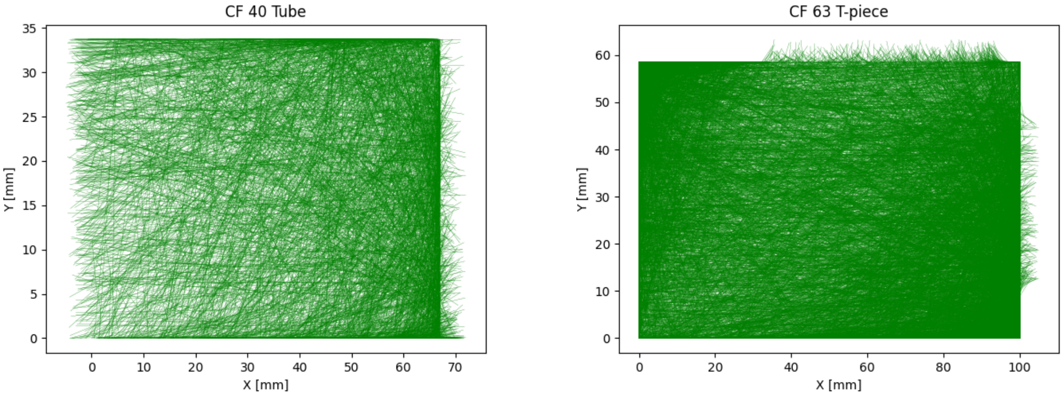

Figure 16: Exemplary images of the simulation after the computation of 1000 particle trajectories.

4.5 Ultra high vacuum

For the ultra-high vacuum section we will carry out the exact same procedure. Assuming that the main source of contamination results from the flux reaching the ultra-high vacuum section from the 2D MOT, we will simulate the particle trajectory from the input to the pump. In terms of geometry, the situation on this side is in principle very similar to the high-vacuum side. We first have a narrow tube (diameter 16 mm, length 74 mm) and then a T-shaped adapter, namely the connector box, which connects the pumping station. The code used to compute the the passing probabilities in the previous section can therefore be re-used. First, once again the results of the narrow tube throughput simulation with five runs and 10.000 particles per run. What we can see in Table 6 is that just as before, the simulation result is $P = 52.02\%$ and thus again much higher, than what was obtained analytically. The theoretical value for the passing probability can again be calculated via 4.30, $P = 20.13\%$. Especially, since the tube is so narrow (16 mm in diameter), the predicted passing probability is very low. But this result is once more only of limited use since the input of the tube is even more narrow than the tube itself, which is why particles have a higher probability to exit the tube through the wider side, which is the output into the connector box. For the pumping stage of the ultra-high vacuum the same simulation as for the high-vacuum part can be run, of course with the updated dimensions and one last time with 10.000 particles in each of the five runs: The estimated passing probability for this last part is $P = 78.25\%$ (see Table 7).

Piece 3	Run 1	Run 2	Run 3	Run 4	Run 5	∅
Pumped [%]	52.00	51.22	52.19	51.88	51.81	52.02
Escaped [%]	48.00	48.78	47.81	48.12	47.19	47.98

Table 6: Simulation results for the connection tube to the connector box on the UHV side

Piece 4	Run 1	Run 2	Run 3	Run 4	Run 5	∅
Pumped [%]	77.86	78.77	78.56	78.55	77.51	78.25
Escaped [%]	22.14	21.23	21.44	21.45	22.49	21.75

Table 7: Simulation results for the connector box

The relatively high passing probability here, as in the last two parts, is the result of the way the arrangement is built. Particles enter the T-shaped piece through a narrow tube and once inside the connector box, the way back through the narrow tube is much less likely than the way up to the pump through a CF40 tube. Thus, once again, the theoretical value for the passing probability obtained with Figure 15 is not of much use, and especially when comparing the total theoretical conductance with the simulated conductance, the discrepancy will become much more exalted. But for the sake of completeness, the theoretical passing probability stands at approximately $P = 35\%$. Applying the series connection formula on this side yields the exact same result as can be seen in 4.31.

4.6 Differential pumping

The differential pumping stage as it was presented in section 3.3.2, serves the purpose of maintaining a relatively constant pressure difference between the two sections of the experimental setup. This is quite simply achieved by making the narrow tube connecting the two parts (see also [26]), and nothing else is in fact the DPS, very small. This way the vast majority of all contaminating particles originating in the region around the atomic beam source will be blocked by said tube and remain in the HV region, where they not only do not interfere with the dysprosium beam on the way to the 3D MOT, but can also be pumped more effectively. When designing the pumping stage, the questions that need to be answered are, what pressure difference should be maintained and what flow conductance is necessary to maintain such a pressure difference. As mentioned in previous sections, we want to achieve around three orders of magnitude difference between the two vacuum regions. An approximation of the required value for the flow conductance C_{DPS} can be given as follows [14]

$$\frac{C_{DPS}}{S} = \frac{p_{UHV}}{p_{HV}} \tag{4.32}$$

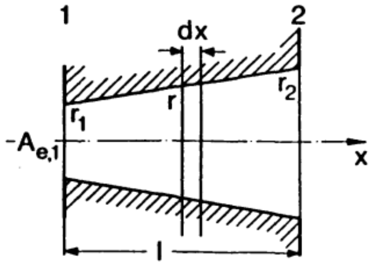

Figure 17: Drawing of a cone shaped tube similar as the linear cross section of our differential pumping stage. Image taken from [23]

Here on the left side we have the ratio between the flow conductance and the pumping speed S. On the right side of the equation is the ratio of the desired pressure in the high vacuum (p_{HV}) and the ultra high vacuum region (p_{UHV}). In our case, with the right hand side of the equation yielding 10^{-3} and the pumping speed being $S = 290$ l/s, as given by *SAES* [12], we conclude, that we need $C_{DPS} \approx 0.3$ l/s or less. In order to be able to tolerate and angled push beam and thus a slightly curved trajectory of atoms from the 2D MOT to the 3D MOT chamber, we decided to have the differential pumping stage cone-shaped. Due to this shape, there is a difference in the passing probability depending whether a particle enters from the more narrow side and passes the element with the probability P_{12} or the other way round P_{21}. The passing probability of a particle entering the tube from the side with the smaller entrance radius can be calculated according to [28]

$$\frac{1}{P_{12}} = 1 + \frac{r_1 + r_2}{4r_2^2} l \tag{4.33}$$

with l the length of the tube and r the respective radii at the beginning and end of the tube, related via $r_2 = r_1 + l \tan\alpha$ with α being the half angle of the cone. The passing probability in case of an entry from the other side is:

$$\frac{1}{P_{21}} = \frac{r_2^2}{r_1^2} + \frac{r_1 + r_2}{4r_2^2} l \tag{4.34}$$

These two equations fulfill the condition

$$A_1 * P_{12} = A_2 * P_{21} \tag{4.35}$$

This means that due to 4.25 the flow conductance is the same either way. It can be seen that the flow conductance of the differential pumping stage is highly sensitive to the radius, so it is best to keep the radius as small as possible. The fact, that the stage can be inserted into the 2D MOT chamber and thus be close to the origin of atomic transport beam of atoms to the 3D MOT chamber helps us in this case. Overestimating the divergency of the atomic beam out of the 2D MOT to around 20 mrad and the distance from the 2D MOT centre to the entry of the DPS, gives us sufficient tolerance if we limit the input radius to 1 mm. The half angle of the cone needs to be larger than the 20 mrad or approximately 1.15° mentioned before, and is therefore set to 2°.

Regarding the length of the cone, there are no pressing constraints from a vacuum point of view. Enlarging the length of the cone will lower the flow conductance, but with less sensitivity than the radius (see 4.25 and 4.34). In order to not over-complicate this custom piece and reduce overall volume of the UHV section, the cone will stretch over the full length of the DPS piece described in section 3.3.2 and therefore be 55.7mm long. Depending on the temperature and the corresponding velocity of particles, the flow conductance of a pumping stage with the described dimensions can be plotted and the result can be seen in Figure 18. As can be seen, within the temperature range that can be presumed once the experiment runs in regular operation, the flow conductance stays below the guideline value calculated above. Temperatures above 450°C will be neither likely nor desirable since it may cause damage to the flange connections sealed by the copper gaskets.

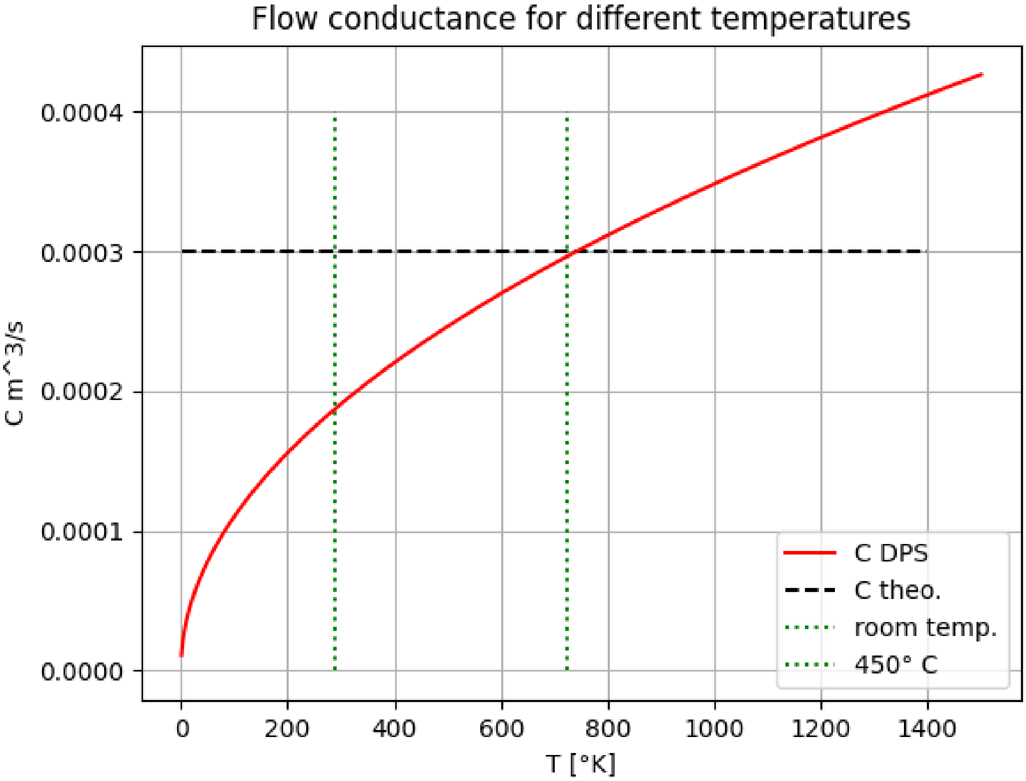

Figure 18: Flow conductance for different temperatures. The black dashed line shows the maximum allowable flow conductance that was calculated above. The two dotted lines frame the temperature region in which the particles will most likely be found during operation, between room temperature and the maximum temperature supposedly allowed for the copper gaskets. Note that the conductance was computed for hydrogen particles, which cause most of the contamination.

4.7 Conclusion

By now we have all necessary components to carry on with calculating the pressures, except for the contamination q_N. This can only be roughly estimated. We know that the dysprosium flux from the oven will be around the order of $4 * 10^{14}$ atoms/s (calculated by Jianshun Gao during the optimization phase of the oven). Since we assume the contamination to be about one order of magnitude less, we fixed the approximate value rather arbitrarily to $4 * 10^{13}$ atoms/s. Note once again that this considers only the main source of contamination namely the oven and does not consider outgassing from the metallic components, neither does it consider any other contaminating particles other than hydrogen, since it is fair to assume that hydrogen will be in fact the main cause for contamination in the chambers. Also one should recall once more, that no adsorption but immediate desorption in a fully elastic manner was assumed. Ultimately it was assumed that due to the narrow entrance towards the ultra-high vacuum section of the experiment, the largest part of the flux will be pumped through the high-vacuum section pumping stage, and only a small part must be considered to contaminate the ultra-high vacuum part. In a simulation run to test this separation, the inside of the 2D MOT chamber was modelled, again this modelling accounted only for the volume of the chamber and the input cross sections of the high vacuum pumping stage and the ultra high vacuum parts. The result was very clear, around 99% of the contamination flux will enter the high vacuum pumping stage, only 1% the ultra high vacuum section. Not only can we see that the effective pumping speed deviates significantly from the speed specified by the manufacturer, but also that the pumping speeds on the two distinguished sides of the experiment differ from each other. The original pumping speed does not include any accounts for the apertures that are built around the pump and of course have limited conductance quality. Furthermore as one can see in 4.25 the flow conductance is quadratically dependant on the radius of the connecting pieces, which is much smaller on the UHV side of the aperture, thus the large difference between the effective pumping speeds on the two sides. As mentioned before, the theoretical approach on calculating the pumping speed yields much smaller values due to the lower passing probabilities for all elements resulting from the geometrical constraints explained above.

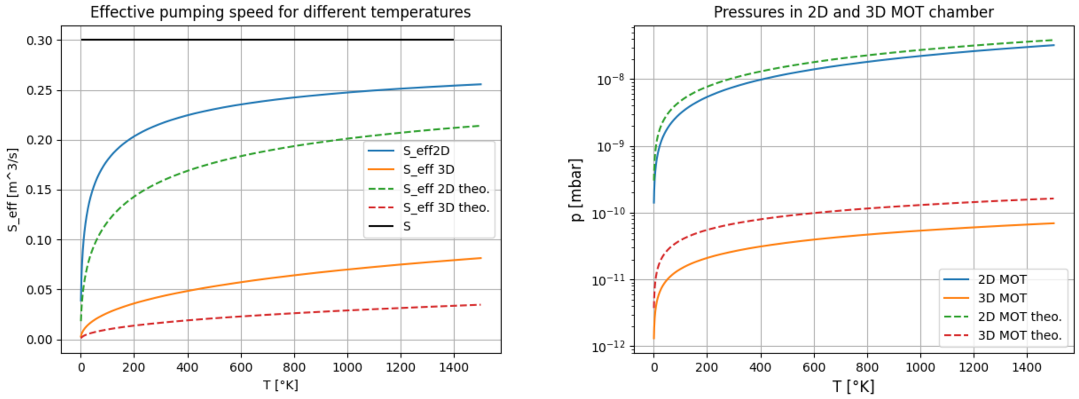

Figure 19: The results of the vacuum calculations and simulations, on the left the effective pumping speed with the theoretical result in the dashed lines and the initial pumping speed given by the manufacturer in black. On the right the pressures for the given contaminating flux. The y-scale is logarithmic here.

On the right hand side of Figure 19, the effective pumping speeds for the high vacuum and ultra high vacuum pumps are plotted. The dashed lines mark the analytically obtained results, the solid ones, the simulation results. One can see that lower theoretical pumping speeds at constant temperature result in a higher pressure. However, pressure is generally more sensitive to temperature (see 4.29) and will rise over the temperature range. The pressure difference, is around three orders of magnitude throughout the temperature range. The temperature range was introduced since it is impossible to assume a fixed temperature over the entire trajectory of the particles and in this way one can get a broader picture of the pressure region we are aiming for with the given geometrical constraints and our vacuum pumps.

Note, that the calculations presented in this section can by no means serve as a precise prediction of the vacuum conditions that will be achieved in the actual experiment, but rather represent one possible way to approach the issue and give a rough estimation of the region we will be reaching with the current setup. However, especially during the process of estimating the mechanical constraints that follow from the vacuum requirements and testing different pump arrangements, the calculations provided a decent overview of the situation.

5 Magnetic field of the 2D MOT

As has been explained in chapter 2.5, in order to apply two-dimensional magneto-optical trapping onto the dysprosium atoms coming out of the oven, we need a spatially dependant magnetic field with a preferably uniform gradient inside the centre region of the 2D MOT. In general there are two ways to achieve such a field, one can use either permanent magnets or coils. Coils have the advantage that the magnetic field can be switched on and off very quickly and precisely depending on the way the power supply is designed. This is especially useful for the magnetic field in the main chamber, for example to tune the scattering length of the atoms through artificially produced Feshbach resonances or separate trapped atom clouds through the Stern-Gerlach effect. The problem with coils is that it is harder, more expensive and more time consuming to produce them, they also require a power supply and sometimes even a water-cooling system, depending on the arrangement of the coils and the power with which they are operated. Permanent magnets are of course not tunable, but they produce a stable and uniform magnetic field and at the same time are cheap and do not take up much space. We therefore decided to use permanent magnets to produce the field in the 2D MOT chamber since there is no need to switch it, but build coils around the main chamber. The work presented in the now following chapter deals solely with the design of a uniform magnetic field for the 2D MOT, using permanent magnets.

When thinking about the setup of the magnetic field, there are only a few simple questions to answer, like what properties we want the field to have, what constraints are there and what is the best possible design to meet both of these criteria decently. The theoretical magnetic field in the 2D MOT, that was used in our capture simulations can be described by:

$$\mathbf{B} = b\mathbf{x} - b\mathbf{y} \tag{5.36}$$

It thus describes a field with a constant gradient b along two perpendicular axes spanning the 2D MOT plane, which is zero in the centre. In our case, these axes should diagonally transverse the 2D MOT chamber along the cooing beams (see 2). This setup creates the desired spatial region in the 2D MOT centre where the atoms are supposed to be confined.

The best value of the magnetic gradient b that is ultimately responsible for the spatial confinement (see 2.5), was to be determined by running the capture simulation and scanning for the maximum loading rate. We know for example from the alkaline mixtures experiment that gradients of around 60 G/cm are used in a 2D MOT with sodium, while only 10-30 G/cm is used in the 2D MOT with potassium [14]. So even for similar atom species, the optimum gradients may vary. In other experiments that are also using 2D MOTs, gradients like 22.5 G/cm for Sr [1] up to more than 50 G/cm for Er [10] and 55 G/cm for Yb [7] are applied, so there is not really a reliable reference pointing towards an optimum gradient region for a 2D MOT of dysprosium.

If the gradient inside the MOT becomes too high, problems can arise, since the Zeeman splitting might not occur linearly anymore, i.e., while in the low magnetic field regime, or the Zeeman regime, the energy levels are grouped according to their hyperfine structure quantum number F and split linearly when a magnetic field is applied, but when the magnetic field becomes stronger, in the Paschen-Back regime, the levels will group according to their respective projection quantum number m_J [24]. This effect is important to consider for experiments with alkaline atoms, since due

to the non-linear energy shift unwanted transitions might be triggered. In the case of dysprosium however, due to the large magnetic moment exalting the Zeeman effect, the magnetic field would need to be ridiculously high to cause problems in that manner.
Since we are for the first time building a 2D MOT with dysprosium, there are virtually no references to turn to when deciding on a specific gradient for the trap, thus we conducted some simulations of our own, to scan for the optimum value in order to achieve a high loading rate. This work was once again carried out by Jianshun Gao. The results was an optimum gradient in the range of 38-46 G/cm. This should at least be achieved within an approximately 50 mm wide region around the centre of the 2D MOT. In that region, the deviation should be as small as possible, meaning the magnetic field in this region is linear.
The challenge is now to find an arrangement of magnets that suits this description. The most common way of achieving this with permanent magnets is to arrange in total four stacks of magnets in a rectangular shape around the chamber (see [1], [2]), with the dipole pointing in opposite directions, so that the field cancels out in the centre of the chamber but creates a uniform linear field along cooling beams. This is also the case in both other experiments at Heidelberg ([13],[14]) that are using the small chamber onto which the permanent magnets can be fixed (shown in chapter 3.3.3). Another option could be to have them fixed on an external mount [2], which might even be adjustable, but if magnets and chamber are built on separate structures, it would probably be harder to align the magnetic field with the cooling beams and the push beam to a distinct region. We therefore decided to have the permanent magnets fixed in the designated spaces described in 3.2.1.

5.1 Permanent magnets

As for the permanent magnets themselves, they should be as compact as possible with a large magnetic moment, so we can achieve the relatively high gradients without needing an exceedingly large amount of magnets. We therefore chose neodymium magnets (*ECLIPSE N750-RB*), which are as well used in many other experiments at Heidelberg and elsewhere (see [1],[20],[13],[14]). Their dimensions are 10*25*3 mm, so they are quite compact, as can be seen in Figure 20. The magnetic dipole lies normal to the large 25*10 mm surface. What is important for the magnetic field design is the magnetization. It was measured by Lamporesi et al. in Turin [20] as well as by Tiecke et al. in Amsterdam [27]. Both measurements are in well accordance with each other, we therefore can conclude that the magnetization of the magnets is around $M = 8.75(10) \times 10^5$A/m. This means that the assumed point like dipole of permanent magnets is around $m = 0.66(1)\mathrm{Am}^2$. The magnets are supposed to work well up to 100°C, which should not be any problem since they are fixed on the outside of the 2D MOT chamber and are therefore shielded from any heat coming out of the oven.

Figure 20: Image of one permanent magnet. The comparison to a one euro coin shows how compact but yet strong the magnets actually are.

5.2 Position scanning

Due to the size of the 2D MOT chamber compared to most other references, the magnets can not be placed as close to the centre as for example in the mixtures experiment in Heidelberg [14]. Since we also preferred to have four extrusions for the magnets on each side of the chamber instead of two, the minimum distance of a magnet to the centre of the large surface of the 2D MOT chamber had to be set to 45 mm, while the distance to the centre plane perpendicular to the push beam axis is 32.5 mm to enable the fixing mechanism introduced in section 3.2.1. This is assuming, that the dipole is concentrated in the middle of one of the extrusion cuts. The actual situation is again slightly different, since the blocks in each extrusion will be composed of multiple magnets, which means they can not all be put in the middle of each cut, but one has to account for a small displacement for each magnetic dipole in order to get a more precise result. While designing the 2D MOT chamber the now following calculations were conducted in order to find an optimum position for the permanent magnet extrusions and to get a more general overview of the magnetic field surrounding the MOT. While the most optimum configuration to copy the magnetic field described by 5.36 would be to have point-like dipoles on the corners of a square. However, neither the square shaped arrangement nor the point-like dipole can be achieved in reality. The field and gradients are simulated using a *Python* script. Therein each dipole is placed at a certain position $\mathbf{r}_0$, creating a magnetic field approximated by

$$\mathbf{B}(\mathbf{r}) = \frac{\mu_0}{4\pi}(\frac{3(\mathbf{r}-\mathbf{r}_0)(\mathbf{m}(\mathbf{r}-\mathbf{r}_0))}{r^5} - \frac{\mathbf{m}}{r^3}) \tag{5.37}$$

This quadrupole approach is sufficient for our purposes [2]. The fields created by each single magnet are then added together. This is conducted for multiple different arrangement concerning the positions of the cuts and the number of magnets in each position. The goal was once to find a configuration with a sufficiently large gradient and as well only a small deviation from this gradient within the centre region. The gradients were calculated along the axes of the oven and the imaging beams, but also along the diagonal axes of the cooling beams.

5.2.1 Four magnets

In the first runs the field was always calculated with a total of four magnet blocks, which are put in the designated spots around the 2D MOT centre. That is, they are located at the positions $(0, \pm y, \pm 32.5\text{mm})$. Different values for y are then scanned, as well as different numbers of magnets per block. In a first assessment to get an overview over the different arrangements, the gradient values at the scanned positions and their respective deviations from the average gradient in the centre region (50 mm around the centre of the 2D MOT, (see 5) were plotted. One can see in Figure 22 that a variety of different gradients is achievable by applying the described 4-block magnet arrangement. The standard deviation of the gradients however becomes smaller for a larger distance from the 2D MOT centre. But even though the gradients along this specific axis are sufficiently high, the

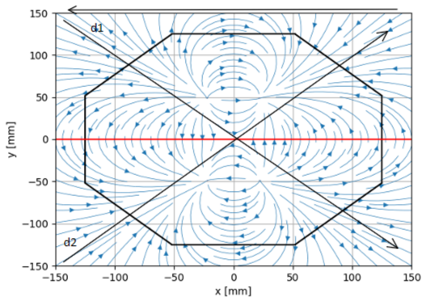

Figure 21: Sketch of the cooling beam path through the 2D MOT chamber. The two orthogonal diagonals span the two-dimensional plane of the MOT.

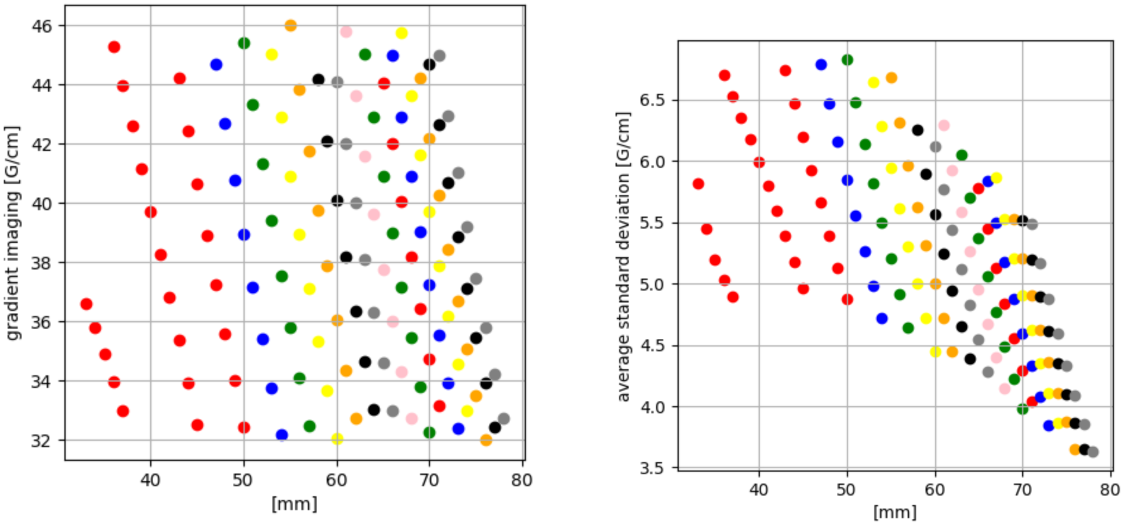

Figure 22: On the left the gradients $\frac{dB_x}{dy}$, so perpendicular to the imaging beam along the vertical axis for different arrangements. On the right the respective deviations for these gradients within the 50 mm wide centre region. Each colour denotes a different number of magnets in a block, from 3, 4 and 5 magnets for three red-dotted lines on the very left up to 19 magnets on the very right.

problem with the 4-block arrangement is, that it can not provide equally high gradients for example along the oven axis or also along the cooling beams. In fact, those along the oven axis are almost half as strong as those along the imaging beam (see Figure 23). The problem is, if the distance between the magnet positions $\pm y$ becomes too large, the field in the middle and along the oven axis becomes too weak. However the goal is that the gradient along all these axes is similar, as it is the case in the proposed theoretical magnetic field (see 5.36). Furthermore not only the strength, but also the orientation of the magnetic field and thus the quantization axis of the atoms does not match the polarization axis of the beams very well anymore. However, this is important for the MOT mechanism (see 2.5). Figure 23 shows more clearly what is meant. The difference between the gradients along the two axes mapped out is about a factor of 0.5. The difference will only increase for larger placement distances, which are preferable due to the smaller deviation from the average. It is also relevant to have a look at the gradients along the paths of the cooling beams. As a reminder, the plan is to have the cooling beams in an arrangement along the diagonals, resembling a 'bow-tie'-like shape, as can be seen in Figure 21. Not only the strength, but also the orientation of the magnetic field and thus the quantization axis of the atoms is relevant. It should match the polarization axis of the cooling beams, this is important for the MOT mechanism (see 2.5). In the theoretical field, the gradients along these diagonal beams should only have a value in the direction of the beam and be zero perpendicular to the beam path. However, with our given constraints this is not achievable in an arrangement with four magnet blocks. In Figure 24, one can not only see how the symmetry of the magnet arrangement plays out, shaping the magnetic fields and the gradients along the two cooling beam diagonals in an inverse way to each other. It also becomes clear that it will be not easy to replicate the theoretical magnetic field with only four magnet blocks. Two values are especially indicative. The average gradient along both cooling beams within the centre region is 30.3 G/cm, so less than 75% of the gradient along the y-axis. Preferably these two gradients should be nearly the same. The second value is the maximum gradient perpendicular to the beams within the centre region, which is 23.7 G/cm. As mentioned earlier this value should be as small as possible. Ideally, the ratio between the average gradients

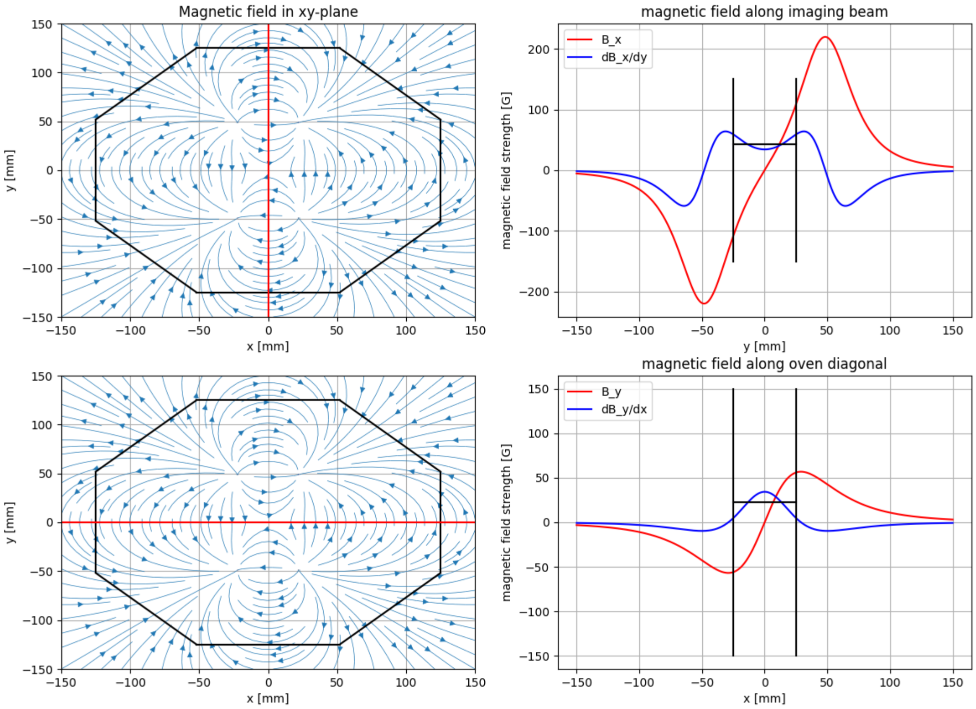

Figure 23: Example of the magnetic field with six magnets per block and the blocks being 48 mm away from the chamber centre. On the left are sketches of the chamber cross section with the magnetic field lines and the path along which the gradients on the right are computed. On the right are plots of the computed magnetic field strengths (red) and gradients (blue) along the path. Also the 50 mm wide centre region is sketched. Within this region the average gradient along the imaging beam in this arrangement is 42.7 G/cm and along the imaging beam 23.1 G/cm.

perpendicular and along the cooling beams should be smaller than one per cent.
Further execution of the scanning process revealed a significant decrease in deviations for all gradients if the permanent magnets are put further away from the 2D MOT centre. Because of the larger distance the graphs in Figures 23 and 24 indicating the field strength and the gradients will be stretched apart and thus be flatter in the centre region. At the same time, however, the total strength of the magnetic field decreases with r^{-3}, so that more and more magnets are necessary to produce sufficient gradients, making the fields directly adjacent to the magnet blocks become very strong, which is also not desirable. Furthermore, with four magnet blocks it is not possible to reduce the ratio between the perpendicular and parallel gradients along the cooling beams to less than 10 %.

5.2.2 Eight magnets

In order to further optimize the magnetic field of the 2D MOT, we decided to try out arrangements with not only four, but eight magnet blocks. The four additional blocks would be arranged in an imaginary rectangle along the oven axis in the same way as the previous four are arranged along the imaging beam axis. Although there are no examples at hand from previous experiments that opted for such a design, we were confident, that it could increase the quality of the magnetic field and therewith the efficiency of the capture process and the overall loading rate substantially. In addition to the four magnet blocks, that were newly added to the simulation, this time the extent of the magnet blocks was also considered. This means that instead of a dipole moment concentrated

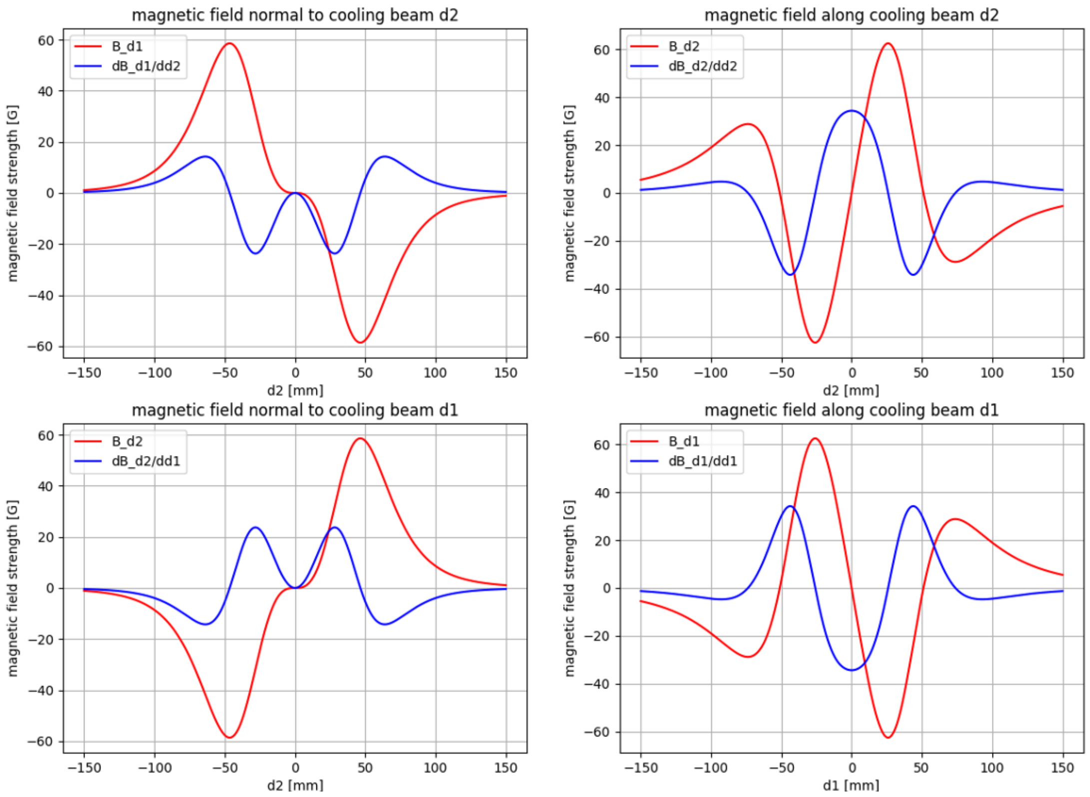

Figure 24: Magnetic fields and gradients along the cooling beam paths for the same arrangement as in Figure 23

at the centres of the designated positions, the simulation now calculated the field of each individual magnet with an increasing positional offset as one goes away from the centre. All fields were again added together and now the result could provide a more precise overview of the total field. The first thing that is noticeable in these revised calculations is that the gradients along the x-axis and the y-axis are now of course equal in strength, but also the gradients along the cooling beams will at least be roughly equally strong. Also the ratio between the gradient along and perpendicular to the beam can be reduced to much less than 10% depending on the exact configuration. So in total, pretty much all objectives can be achieved in this arrangement. Still the exact positioning had to be chosen. Running the positioning scanning with respect to the minimum standard deviation for eight magnet blocks yielded a slightly different result than previously shown in Figure 22. As can be seen, the deviation decreases drastically when going from very close distances further away, but at around 55 mm, it reaches a sort of valley, but still decreases slightly. Note that the deviation in this plot is the average of the standard deviation of all the different gradient paths taken into account. When going through the exact data, one can see, that even though the deviation along the coordinate axes is minimal at around 54 mm, the deviation along the diagonal beams is much larger there and overlays this effect.

So in general we want to be far away from the centre, the maximum possible distance is about 80 mm. However, then it will get very hard to create a sufficiently strong field and many magnets are required, which can also influence other parts of the assembly. Therefore the positioning of the magnet blocks was ultimately chosen to be: $(\pm 63, 0, \pm 32.5)$ [mm] and $(0, \pm 63, \pm 32.5)$ [mm]. Here it should be easy to achieve gradients of more than 40 G/cm with only eight or nine magnets per block and the gradients along coordinate and diagonal axes are especially close to each other. In Table 5.2.2 one can seen an overview of the achievable gradients with eight stacks of permanent

n	Grad. xy-axes. [G/cm]	Grad. diagonal [G/cm]	Ratio	Avg. dev. [G/cm]
6	31.97± 0.67	31.52 ± 1.42	∼1%	0.78
7	36.72±0.71	36.72 ±1.69	∼1%	0.93
8	41.24±0.73	41.9±1.97	∼2%	1.10
9	45.49±0.72	47.06±2.28	∼2%	1.28

Table 8: Overview over the average gradients, deviations and strength ratios between the gradient parallel and perpendicular to the diagonal axes for different numbers n of single magnets per block.

magnets, each placed at a position 63 mm away from the centre axis of the 2D MOT chamber.

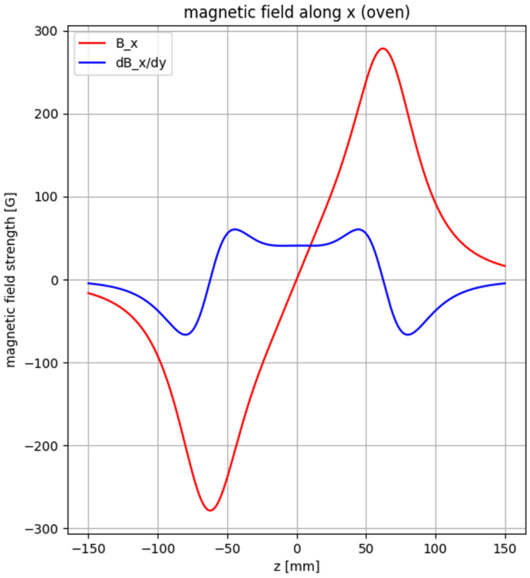

Figure 25: Final magnetic field (red) and its gradient (blue) along the x-axis with eight magnet blocks (n=8). Due to the symmetric arrangement, it is the exact same as along the y-axis.

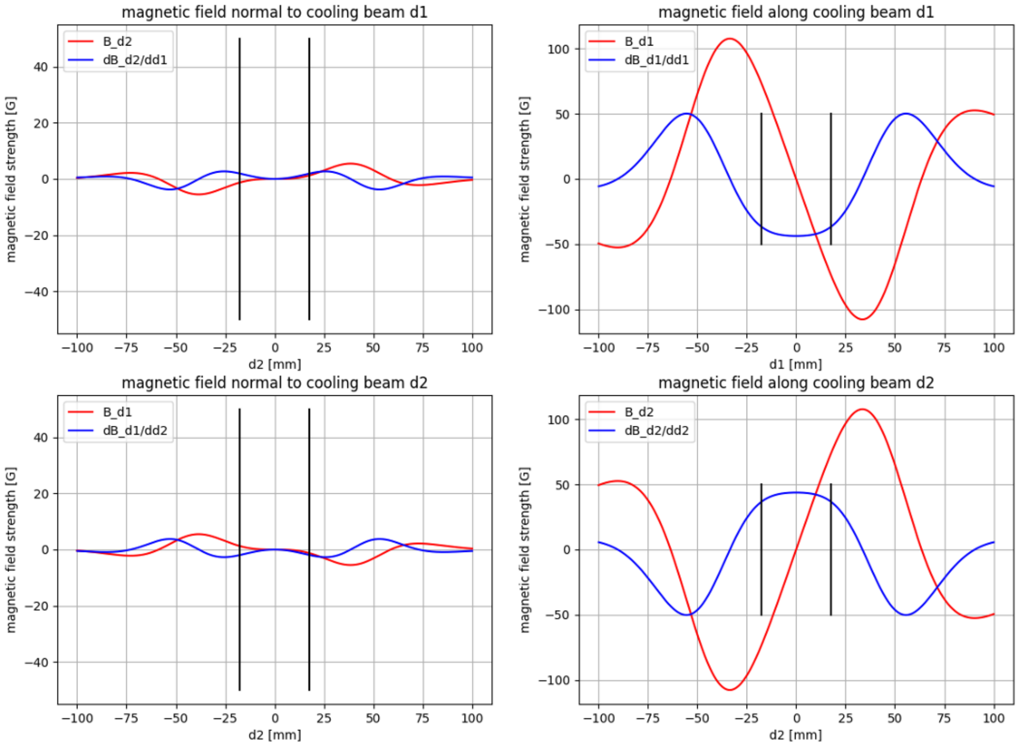

Figure 26: Final magnetic field with eight magnet blocks parallel and perpendicular the diagonal cooling beams (n=8).

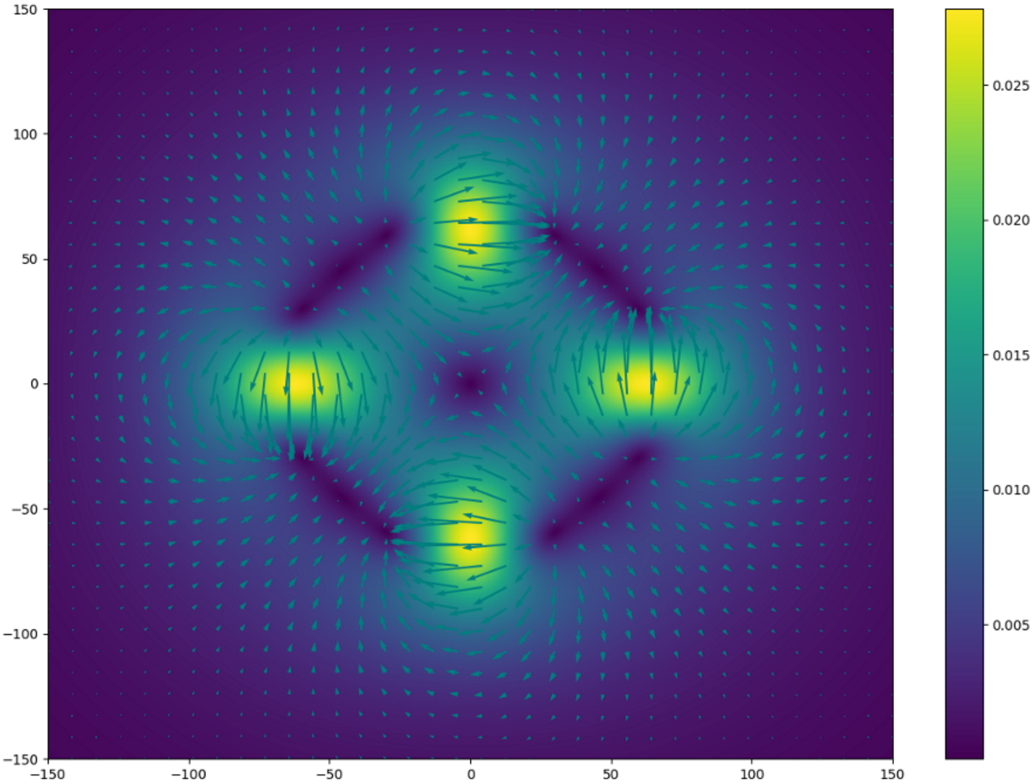

Figure 27: Final magnetic field with eight magnet blocks. A schematic view onto the 2D MOT plane.

5.3 Asymmetric arrangements

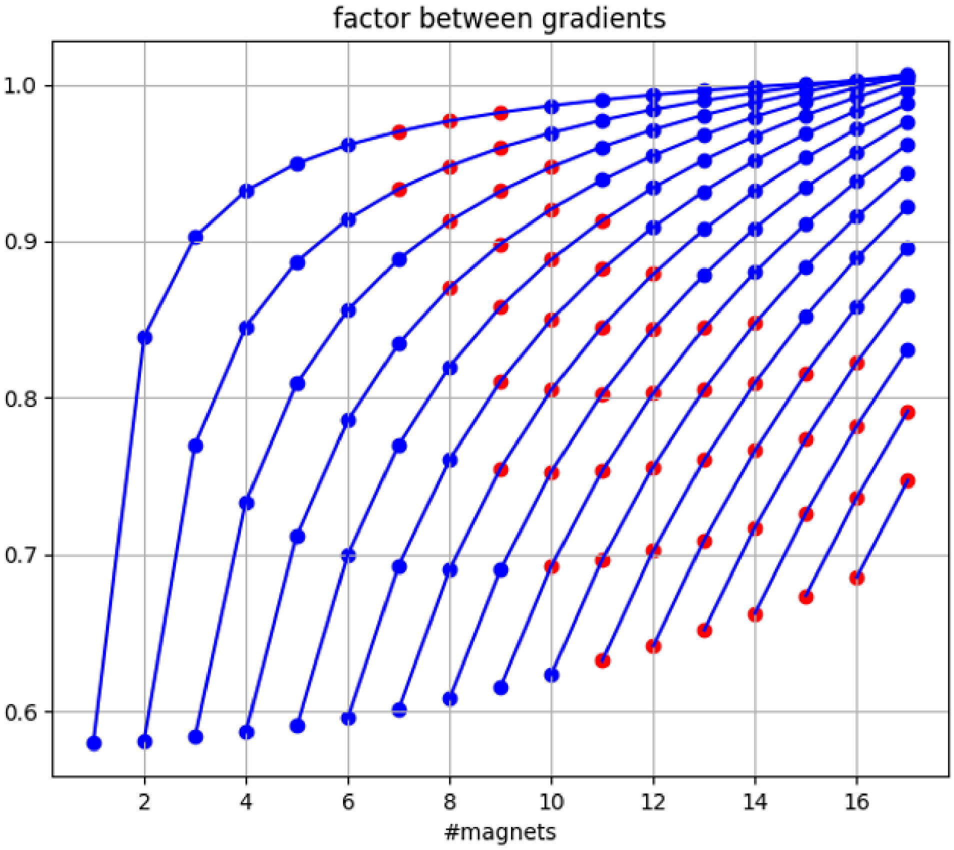

Figure 28: Full scan of the asymmetric field arrangement options. Each line depicts a certain magnet number of difference between the axes. The red dots are those arrangements that provide sufficient gradients. For example, the dot at (6, 0.7) is in the fifth line from the left, meaning an arrangement with five magnets difference, so six along one axis, one along the other has a factor of 0.7 between the gradients.

During the tests for the loading rate, we eventually encountered the possibility that a non-symmetric magnetic field might in fact be beneficial to the loading rate. Even though we were not exactly confident in this result especially due to the quantization-polarization problem mentioned in 5.2.1, the modular design of our magnet holders allows us to easily change the number of magnets in certain blocks and to create an asymmetric field. So we just conducted some tests to check what level of asymmetry we can potentially achieve while maintaining the necessary field strength, and how it changes when removing an arbitrary number of magnets. So actually what we tested now was what happens if we take a small step back and have an arrangement with two times four blocks, but different number of magnets in the blocks aligned with different axes. For this trial we simply reduced the number of magnets in the stacks aligned with one of the coordinate axes and ran the simulation again. The primary measure for asymmetry was chosen to be the factor between the smaller and larger gradient. The smaller this factor or ratio, the larger the difference in gradients. If the factor is one, the gradients are the same. From the tests with four magnets, we could already estimate that a factor of 0.5 between the two is roughly the lower limit. When running the new simulation, we in fact realized that for magnet number differences up to five, the factor stays larger than 0.85. It decreases rapidly for a smaller total number of magnets, but then also the gradients are in general too small to operate a 2D MOT. So we only take those arrangements into account, where we actually cross the minimum threshold of 36 G/cm. A full summary of the test results can be seen in Figure 28.

Even though the test result shows some decent options for non-uniform magnetic fields with a factor of down to about 0.65, it should be noted that such arrangements generally bring a larger total average deviation with them. For this reason and also due to the lack of references where such a field has been tested in an actual experiment, we will most likely first start operating our 2D MOT with a symmetric magnetic field configuration, like those presented in 5.2.2. According to the conducted field and gradient simulations and in accordance with Jianshun's loading rate simulations, the $n = 8$, eight magnet blocks symmetric arrangement, as it can be seen in Table 5.2.2 seems to be the most promising one for our purposes.

5.4 Unwanted effects

In the whole assembly of the experiment, there are multiple sources of electro-magnetic fields. They all serve a specific purpose, but are otherwise nothing more than a disturbing factor in an experiment that requires high precision. Neglecting all minor field sources like electronics setups around the experiment or stray light in the setup, there are mainly four sources, producing a magnetic field. Two Ion-Getter vacuum pumps and two MOTs. As for the Ion-Getter pumps, it has been mentioned in section 4.2.2 how the magnetic field is necessary for their operation. Inside these pumps the magnetic field is actually quite strong in order accelerate electrons and ions, such that ionizing collisions occur. However, the pumps are provided with magnetic shielding on five sides. Also the manufacturing company could provide us with more detailed data sheets depicting the strength and decrease of the field from the connecting flange. It appears that after only 10 cm, the magnetic field genrally decreases to less than 0.5 G and the gradient is almost completely flat. Taking a look at our assembly in Figure 4, we see, that the flange connection of both pumps is much further away from the central axis of the experiment than only 10 cm (around 16 and 18 cm respectively). It is this axis along which the atoms are pushed and which must therefore be especially protected from unwanted influences.

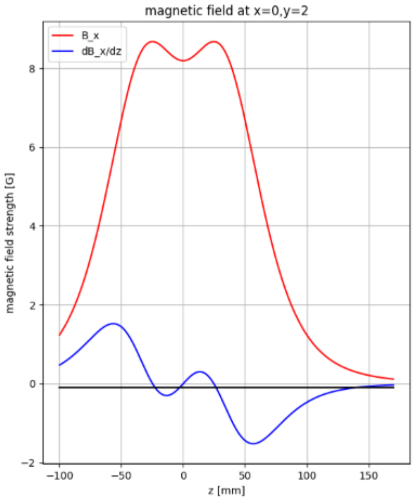

Figure 29: Plot of the decrease of the magnetic field along the push beam axis with an offset of 2mm.

The previously described field of the 2D MOT might have some influence onto the transport mechanism of atoms from the 2D to the 3D MOT via a laser beam with a small waist, pushing the atoms along the z-axis, hence it is also called 'push-beam'. The transport mechanism operates via atom-light interaction in a similar way as described in chapter 2, but without a magnetic field. There is, however, a magnetic field in close proximity, which is why we should check the strength of the field and its gradient along the z-axis and in a cylindrical area around it. Due to the symmetric arrangement, the field vanishes exactly on the z-axis, but does not vanish in a small region around it. Right along the axis, symmetry dictates, that the separate fields of the magnets will be opposed and cancel each other out. The push beam has a waist of up to 2mm and as soon as one goes slightly above or beneath the central axis, the magnetic field will not vanish anymore. As mentioned in the chapter on the mechanical design 3.3.1, the push beam will also have a small tilting angle, but since this angle is with a maximum of around 4.5° very small, we will ignore it for simplicity and just for now look at how the field behaves within a cylindrical region around the central axis, with a radius of 2mm.

In the plots one can clearly see the two maxima of the magnetic field at the respective positions of the magnet blocks 32.5 mm away from the centre. It is also noticeable that the gradient is much smaller than the actual field, less than 2 G/cm. Moving even further away from the centre, the gradient decreases even more, reaching less than 0.1 G/cm around 15 cm away from the centre. This is of particular interest, since at the small connector box's viewports 17-18 cm from the 2D MOT centre, there is the option to shape the atomic beam further before it enters the main chamber. This process will principally work with the same atom-light interaction mechanics introduced in chapter 2, thus a magnetic field can influence the process. But the decline of the 2D MOT field seems sufficient enough as to not disturb this in any way. The design of the magnetic field for the main chamber is based on coils and is still being developed. It is, however, reasonable to assume that the produced fields and gradients will be much smaller than in the 2D MOT chamber and therefore should not cause any problems.

6 Conclusion and Outlook

6.1 Conclusion

This thesis covered some of the first thoughts and first design ideas and steps to build a new ultracold atom experiment with the goal to produce dipolar quantum gases. Namely the mechanical design, vacuum pumping and 2D MOT magnetic gradient calculations. What is in particular special is our plan to work with a 2D MOT for dysprosium, which has never been accomplished before, although there are various examples of similar experiments with dysprosium or dysprosium mixtures.

It should be noted that the contents of this thesis and the thoughts presented therein concerning the experiment are at the time that this thesis is completed actually nothing more than that, thoughts. Over the course of the months during which all the design drawings and simulations presented in the thesis were created, we at the same time continuously worked on establishing a new research group at the Physical Institute of the University of Heidelberg. This means that not only an office space, but especially a new laboratory had to be set-up and be adapted to the needs of our experiment. It also means that even though our lab has already transformed significantly compared to the state of a few months ago, we are still weeks away from actually starting to built up the vacuum system. For now the whole experimental assembly exists only in a digital format. However, since we are building a new precision experiment, it has been crucial to test and discuss the most critical parts of the experiment in depth before actually building it. As for the mechanical parts, the general setup of the experiment and the process of developing certain customized parts were explained in detail in chapter three (3). Especially the constraints following from the properties of dysprosium and the requirements that we imposed upon ourselves played a crucial role. They are also the reason why the final design looks quite different from all other experiments already existing in Heidelberg that we were actually able to look at in person. Of course the main differences are related to the size of our dysprosium oven. All other experiments in Heidelberg are working with alkaline metals and can use much smaller ovens. This contributes greatly to the general compactness of the other experiments. While we also focus on reducing the size of the

apparatus, the vacuum structure is larger than our references [14] and [13], but yet comparably compact. Since we are for now also not planning to connect a Zeeman-slower, we can in fact even have a slightly smaller setup than other heavy atom quantum gas experiments. Even though the general shape of the 2D MOT chamber is fairly simple, we tried to optimize it further and further over the course of many weeks, since it is one of the most important core parts of the experiment. The other part, that was significantly changed compared to other experiments in Heidelberg ([13],[14]) is the pumping and pushing stage, since it had to be made wider to allow the input of an angled push beam. It was another limitation resulting from the properties of dysprosium. Apart from that, many parts were designed in a similar way as in the HQA, such as the connector box. However, the structure of the vacuum differs. This is because, in order to achieve more effective transport of the atoms into the main chamber, we have chosen to place the differential pumping stage as close as possible to the center of the 2D MOT, while in the HQA it is located behind the gate valve to ensure more effective vacuum pumping. Also instead of a glass cell, we are including a metal science chamber into the experiment, at least for the first intermediate time stage.
As for the vacuum chapter 4, as mentioned earlier, the goal was to find a way to estimate the quality of the vacuum during normal operation, assuming that there are no pumps other than the Ion-Getter pumps and that there are no leaks. In this way, different designs for the vacuum parts could be tested in order to optimize the setup also in terms of vacuum quality. Especially for the pumping and pushing stage as well as for the differential pumping stage, these tests were applied very frequently for different design ideas and contributed a lot to the final shape of these parts. To sum up, we are confident, that with our currently planned setup we will manage to reach pressures in the range of $10^{-8} - 10^{-9}$ mbar in the high-vacuum section and pressures down to around 10^{-11} mbar in the ultra high vacuum section. Measures typically used to support vacuum generation, such as bake-out to reduce the outgassing rate of materials, were not part of this thesis.
Ultimately the fifth chapter is concerned with the setup of the magnetic field for the 2D MOT chamber. Again since this is the first time a 2D MOT for dysprosium is built, we took special care designing the magnetic field and simulated a lot of different magnetic field arrangements. In fact the difference compared to all of these references such as [2], [1] or [15] is that we decided to use eight magnet blocks instead of four because it is easier to achieve high gradients with fewer magnets per block and the field is more homogeneous. Also a brief test of possibly beneficial non-symmetric arrangements was conducted, but will likely not be implemented in the MOT. Finally we looked at the unwanted sources of electro-magnetic fields, that might possibly influence the experiment.
Overall we covered the turbulent first months of setting up a new research experiment and laid some foundations on which further parts can be built and improvements can be made.

6.2 Outlook

There are a lot of things yet to be done, before we can commence the operation of the experiment. To name just a few examples: The entirety of the optical setup, which was also not part of this Bachelor project has to be designed. This includes beam paths for cooling beams of both MOTs, the push beam and imaging beams. Then there is also the coil-based magnetic field of the 3D MOT that needs to be built, and the Dipole trap into which atoms are supposed to be loaded ultimately, which in turn requires a laser setup. Even with an existing plan that shows how to implement all of these things, a control system is still needed for the various parts of the experiment. This project includes software and hardware issues, that range up to such questions as where to setup the control panels in the lab and the subsequent requirements for the lab space. While most of the things mentioned above are matters to be worked on from an office space we also plan to spend more and more time on the organization of the laboratory. This includes ordering all sorts of necessary standard parts and finally also the custom vacuum parts and once all necessary components arrived we can start with building the vacuum structure itself and proceed with measures to improve the vacuum quality and also measurements of the magnetic field.

To sum up, there is much more to come and much more to talk and write about than what can be done within the extent of a Bachelor's thesis.

References

[1] M. Barbiero. *Novel techniques for a Strontium Optical Lattice Clock*. PhD thesis, Politecnico di Torino, 2019.

[2] E. Casotti. A two-dimensional magneto-optical trap for strontium. Master's thesis, Ludwig-Maximilians-Universität München, 2020.

[3] Paolo Chiggiato. Materials and properties iv. Technical report, CERN Accelerator School (CAS) on Vacuum for Particle Accelerators, Geneva, Switzerland, jun 2017.

[4] Miller Electric Mfg. Co. *Guidelines for Gas Tungsten Arc Welding (GTAW)*. Miller Electric Mfg. Co., Appleton, Wisconsin, USA, 2013.

[5] J. Dalibard. Une brève histoire des atomes froids, 2014-2015.

[6] S. Donadello. *Observation of the Kibble-Zurek mechanism in a bosonic gas*. PhD thesis, University of Trento, 2016.

[7] S. Dörscher and K. Sengstock et al. Creation of quantum-degenerate gases of ytterbium in a compact 2d-/3d-magneto-optical trap setup. *Review of Scientific Instruments*, 84(043109), 2013.

[8] S.E. Dörscher. *Creation of ytterbium quantum gases with a compact 2D-/3D-MOT setup*. PhD thesis, Universität Hamburg, 2013.

[9] C.J. Foot. *Atomic Physics*. Oxford University Press, 2005.

[10] A. Frisch. *Dipolar Quantum Gases of Erbium*. PhD thesis, Universität Innsbruck, 2014.

[11] Pfeiffer Vacuum GmbH. *The Vacuum Book Vol. 1*. Pfeiffer Vacuum GmbH, 2008.

[12] SAES Group. *NexTorr UHV pumps*. SAES Group, Lainate, Milan, Italy, 2020.

[13] T. Hammel. Design and construction of a new experiment for programmable quantum simulation using ultracold ^{6}li fermions. Master's thesis, Universität Heidelberg, 2021.

[14] L. Höcker. Building up a modular na-k quantum gas experiment. Master's thesis, Universität Heidelberg, 2019.

[15] P. Ilzhöfer. *Creation of Dipolar Quantum Mixtures of Erbium and Dysprosium*. PhD thesis, Innsbruck University, 2020.

[16] P. Ilzhöfer and F. Ferlaino et al. Two-species five-beam magneto-optical trap for erbium and dysprosium. *Physical Review*, 97(023633), 2018.

[17] S. Jin. *A New Generation Experiment for the study of strongly Interacting Fermi gases*. PhD thesis, Ècole Normale Superieure, Paris, 2019.

[18] K. Jousten et al. *Handbuch der Vakuumtechnik*. Springer Verlag, 2018.

[19] J. Kluge. Design of a zeeman slower for a second generation experimental setup on quantum degenerate dysprosium gases. Master's thesis, Universität Stuttgart, 2019.

[20] G Lamporesi, S Donadello, S Serafini, and et al. Compact high-flux source of cold sodium atoms. *Review of Scientific Instruments*, 84(063102), 2013.

[21] H.G. Metcalf and P. van der Straten. *Laser Cooling and Trapping.* Springer Verlag, 1999.

[22] K.A. Mohammad, A. Ali, B.B. Sahari, and S. Abdullah. Fatigue behaviour of austenitic type 316l stainless steel. *IOP Conf. Series: Materials Science and Engineering*, 36(012012), 2012.

[23] J. F. O'Hanlon. *A User's Guide to Vacuum Technology.* John Wiley and Sons, 2003.

[24] D. A. Steck. Sodium d line data. *available online at http://steck.us/alkalidata*, 2019.

[25] J. Thompson et al. Narrow-line cooling and imaging of ytterbium atoms in an optical tweezer array. *Physical Review Letters*, 122(143002), 2019.

[26] T. Tiecke. *Feshbach resonances in ultracold mixtures of the fermionic quantum gases* ^{6}Li *and* ^{40}K*.* PhD thesis, Universiteit van Amsterdam, 2009.

[27] T.G. Tiecke, S.D. Gensemer, A. Ludewig, and J.T.M. Walraven. High-flux two-dimensional magneto-optical-trap source for cold lithium atoms. *Physical review*, 80(013409), 2009.

[28] M. Wutz, H. Adam, and W. Walcher. *Theorie und Praxis der Vakuumtechnik.* Vieweg, 1992.

Acknowledgements

At this point I would briefly like to thank a few people, who have been supporting me over the course of this thesis. First and foremost, I would like to thank my supervisor Lauriane Chomaz for giving me the great opportunity of helping to design a whole new experiment from the very start. Thanks also to Selim Jochim for taking over the second correction. A great thank you to the whole Quantum Fluids team for hours of inspiring discussions about major, or also minor issues. A great thanks to Jianshun Gao in particular, who not only through his work laid down a framework onto which multiple parts of this thesis were built, but who was also always happy to help me with all sorts of issues, be it directly related to the work or let's say only loosely connected. Thanks also to the HQA Team, in particular Tobias Hammel and Armin Schwierk, who were always happy to discuss problems we encountered on the way and to share their experiences with us. Thanks in that manner also to Lilo Höcker and the alkaline mixtures team at the KIP.
A big thank you for many great evenings to my friends here in Heidelberg, especially my (former) flatmates Juri, Tobi and Patrick.
Last but not least, I would like to thank my amazing girlfriend Rahel as well as my family for their unconditional support and advice whenever I needed it.

Erklärung

Ich versichere, dass ich diese Arbeit selbstständig verfasst und keine anderen als die angegebenen Quellen und Hilfsmittel benutzt habe.

Heidelberg, den 12.10.2021,